Fall 2023

Application of Overburden Effects to the Elastic Scattering Limit for CDMSlite Run 3

Michael Litke
Southern Methodist University, litkem@smu.edu

APPLICATION OF OVERBURDEN EFFECTS

TO THE ELASTIC SCATTERING LIMIT FOR CDMSLITE RUN 3

Approved by:

Dr.Jodi Cooley
Professor of Experimental Particle Physics

Dr.Roberto Vega
Associate Professor of Theoretical Physics

Dr.Joel Meyers
Assistant Professor

Dr.Durdana Balakishiyeva
Lecturer

Dr.Robert Calkins
Research Assistant Professor

APPLICATION OF OVERBURDEN EFFECTS TO THE ELASTIC SCATTERING LIMIT FOR CDMSLITE RUN 3

A Thesis Presented to the Graduate Faculty of the

Dedman College

Southern Methodist University

in

Partial Fulfillment of the Requirements

for the degree of

Master of Science

with a

Major in Physics

by

Michael Litke

B.S., Physics, Brandeis University

December 16, 2023

Acknowledgments

I would like to thank my advisor Jodi Cooley, who is the reason I came to SMU and has gone above and beyond to help me succeed here, especially during my most difficult moments during the pandemic. Without your support, especially in navigating the process of applying to programs again, I would not have made it this far.

In the same spirit I want to thank Steve Sekula for his incredible support of myself as well as the other graduate students in this time as chair of the department.

I would also like to profoundly thank Rob Calkins, who has been an extremely patient guide for me in learning an analysis that was completely new to me. You've been extremely helpful and I feel I would never have finished this work in time without your assistance.

This work was funded by the Nation Science Foundation under award number 2113835

Litke, Michael B.S., Physics, Brandeis University

Application of Overburden Effects
to the Elastic Scattering Limit for CDMSlite Run 3

Advisor: Dr.Jodi Cooley
Master of Science degree conferred December 16, 2023
Thesis completed August 2, 2023

Many different types of astronomical evidence suggest that most of the mass in the universe is attributable to a nonluminous matter, called dark matter by physicists. Dark matter is believed to be one or more new elementary particles with currently unknown properties. So far, the prevailing method for attempting to discern the properties of the new particle(s) is to observe a direct collision between dark matter and standard model particles.

SuperCDMS is a direct detection experiment conducted underground that measures ionization and phonon energy in cryogenic germanium crystal detectors. While taking data in the CDMSlite configuration it can amplify the ionization signal, dramatically lowering the threshold for a detectable amount of energy deposited in the detector via a collision with a hypothetical dark matter particle.

Previous analysis of data taken in the CDMSlite mode examining the elastic scattering limit disregarded any energy loss due to the dark matter passing through the earth and atmosphere to reach the detector. The practical effect of this energy loss is that any dark matter particles which have very high interaction cross sections with normal matter ($\sim 10^{-30}\mathrm{cm}^2$) will have lost too much of their energy to be detectable by the experiment once they have reached it. This work will describe a method to account for this effect and present a re-analysis of the CDMSlite run 3 data, resulting in an adjusted sensitivity band, rather

than just a lower limit. The lower limit of the new band is consistent with the previously published lower limit obtained without incorporation of the overburden. The upper limit is consistent with the previous limits from other experiments, with an upper limit on the cross section of 10^{-31} cm^2 for a 1.5 GeV WIMP.

TABLE OF CONTENTS

LIST OF FIGURES ix

LIST OF TABLES xii

CHAPTER

1 Introduction 1

1.1. Evidence for Particle Dark Matter 1

1.2. Particle Dark Matter 4

1.3. Detection of Dark Matter 5

1.3.1. Direct Detection of Dark matter 6

1.3.2. WIMP Rate 9

1.4. Strong Dark Matter and Windows in Parameter Space 11

2 The SuperCDMS Experiment 13

2.1. The CDMS Experiments 13

2.2. SuperCDMS Soudan 14

2.2.1. Shielding and Overall Configuration 14

2.2.2. The iZIP detectors 16

2.2.3. CDMSlite 18

3 CDMSlite run 3 Analysis 21

3.1. Data 21

3.1.1. Data used in this analysis 21

3.1.2. Overview of data quality cuts 22

3.2. Background Modeling 26

3.2.1. Surface background models 27

3.2.2. Background Morphing 30
3.3. Efficiency 34
3.4. Resolution 34
4 Overburden 38
4.1. Theory 38
4.1.1. Practical Considerations 40
5 Profile Likelihood Analysis 44
5.1. Likelihood functions 44
5.1.1. General Introduction 44
5.1.2. The Likelihood function for this analysis 46
5.2. The Limit Calculation 48
6 Results 52
6.1. Outlook 53
BIBLIOGRAPHY 55

LIST OF FIGURES

Figure Page

1.1 The rotation curve for NGC 6503 [6]. The black points are the measured velocity plotted as a function of radius. The observed rotation curve cannot be accounted for by the models we have for luminous matter and non-luminous gas alone. Dark matter is required to be consistent with the data. . . . 2

1.2 The Bullet Cluster [9]. This image is color coded with the red areas being the luminous mass composed of standard model particles and the blue showing where the dark matter is inferred to be from weak lensing. . . . 4

1.3 A survey of the signals produced by a dark matter event and the technologies used to read them out [12] . . . 7

1.4 The limits of several selected direct detection experiments. The yellow area represents the solar and cosmogenic neutrino background. Below the dashed line the neutrino background becomes comparable to the dark matter signal and severely limits sensitivity, as under current technology there is no way of distinguishing between dark matter scattering events and neutrino scattering events. They greyed out area above each curve is the area excluded by that experiment, as none have so far made a discovery. Some of the above limits have upper bounds as well as lower bounds, and for those limits the area above the upper bound is not excluded. . . . 9

1.5 Some constraints placed on dark matter properties from cosmological observations [20]. . . . 12

2.1 Side view of the shielding layers around the Soudan experiment [28] . . . 15

2.2 A typical resistance curve for a TES. There is a sharp transition after what is known as the critical temperature which allows a very clear readout for when an event happens. . . . 17

3.1 The electric field configuration for the detector. As this plot shows, for high radius events the E-field is non-uniform. Green regions are areas where the experienced bias voltage is less than that in the bulk; in this case 70 V [33] . . . 24

3.2 Surface backgrounds for all three sources from R3a (left) and R3b (right). The orange curves represent the systematic error on the voltage map used in the simulation and the green lines represent the systematic error of the voltage cut location. The black median curve has been scaled to a pdf with unit area and is shown with statistical error bars. The green and orange lines have been scaled to maintain the ratio with the black curve, and the blue curves are the quadrature sum of the statistical and systematic errors. 29

3.3 Morphing the event density model of surface events from the copper top lid for R3a (left) and R3b (right) 31

3.4 Morphing the event density model of surface events from the copper sidewall housing for R3a (left) and R3b (right) 31

3.5 Morphing the event density model of surface events from the germanium crystal for R3a (left) and R3b (right) 32

3.6 Histograms of the number of events from Gaussian sampling of the top lid morphing parameter (left), sidewall morphing parameter (center) and germanium morphing parameter (right) 33

3.7 Plots of the number of total events from top lid (left), sidewall (center) and germanium (right) as a function of their respective morphing parameters .. 34

3.8 The efficiency curves for R3a (left) and R3b (right) morphed between$m =$ -1 and $m = 1$ 35

3.9 The blue points are the measured resolutions of the baseline noise and germanium activation peaks. The black curve is the best fit of the resolution model, and the orange band is the uncertainty of that fit. The top plot shows the measured peaks up to 11 keV, while the lower plot is zoomed in below 1.5 keV. The left figure is the resolution curve for R3a, an the right figure is the resolution curve for R3b 36

4.1 The effects of passing through a single layer on the velocity distribution for $m_\chi = 1$ GeV, $\sigma_{\chi n} = 10^{-30}$ cm^2 [39] 40

4.2 The coordinate system used to calculate the damping factor 41

4.3 The variation of the damping parameter with the angle of approach shown for a fixed cross section and linearly varied mass(left) and a fixed mass and linearly varied cross section(right). We can see that the parameter is linear in cross section and depends exponentially on the mass. We can also see the features of the model of the Earth used for these calculations. The first kink represents the boundary between the core of the Earth and the mantle, and the second kink represents when the dark matter only passes through the rock around the detector, which is why the parameter has a nearly constant non-zero value there. 42

4.4 How the different velocity distributions vary with their angle of approach to the detector. 42

4.5 Geology surrounding the Soudan mine 43

5.1 an example scan of a test statistic through parameter space. The red point is the unconditional best fit 50

5.2 Two example scans, one showing a point included (left), one excluded (right) . . 51

6.1 The updated exclusion band for CDMSlite run 3 (shaded in red), along side the limits set by a selection of other recent experiments, as well as the neutrino floor shown in yellow 52

LIST OF TABLES

Table Page

3.1 The measured resolutions of known features in the data (top), resolution model parameters from fitting to the measured widths (middle), and correlations between the model parameters (bottom). 37

5.1 Table of the variables used in the likelihood function 46

Chapter 1

Introduction

1.1. Evidence for Particle Dark Matter

The oldest pieces of evidence for the existence of dark matter derived from astronomical observations are the velocity dispersions of stars within galaxies and galaxies within galaxy clusters. Going back to Lord Kelvin the velocity dispersions of stars (treated as a non-interacting gas of particles under the influence of gravity) have been used to estimate the total dark mass in their galaxies, although Kelvin and the scientists who followed him thought that the non-visible mass was baryonic matter like "cool and cold stars, macroscopic and microscopic solid bodies, and gases" [1] until the 1980s. The first person to apply velocity dispersion techniques to galaxy clusters was Fritz Zwicky. He did so in two papers in 1933 [2] and 1937 [3], coming to the conclusion that there was much more mass than could be accounted for by stars and gas. This surprising result motivated further research into more galaxy clusters such that by the early 1960s it had been established that dark matter made up the great majority of the mass in all galaxy clusters.

The next big line of evidence was established in the 1970s. In 1970 Vera Rubin and Kent Ford used an image tube spectrograph developed by Ford to measure the rotation curve of the Andromeda galaxy with a significantly higher accuracy than had been achieved before and found that it was flat out to large radii [4]. Rubin and Ford followed this up in 1978 by applying the same techniques to many more spiral galaxies and providing definitive evidence of what would become known as the galaxy rotation problem, that the outer regions of galaxies rotated fast enough that without the addition of unseen matter they would fly apart [5]. One such rotation curve can be seen in Fig. 1.1. Assuming that our understanding of gravity on macroscopic scales is correct, these curves imply that there is additional mass interacting gravitationally with the matter that we can see.

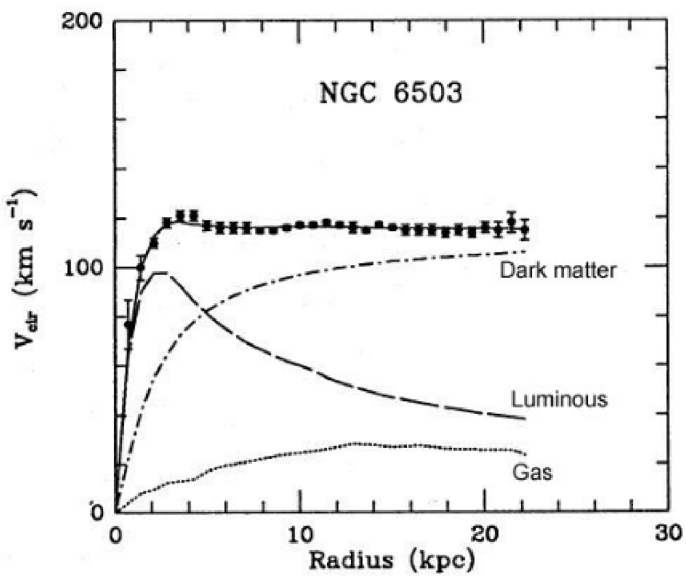

Figure 1.1: The rotation curve for NGC 6503 [6]. The black points are the measured velocity plotted as a function of radius. The observed rotation curve cannot be accounted for by the models we have for luminous matter and non-luminous gas alone. Dark matter is required to be consistent with the data.

In addition to astronomical evidence pointing towards the existence of unseen matter, the Cosmic Microwave Background (CMB), also provides strong evidence pointing towards this hypothesis as well. The CMB represents the surface of last scattering of light during the very early period of the universe when electrons and protons were too hot to form hydrogen atoms, at which point they became electrically neutral and stopped scattering with photons. The temperature that we measure at any given point on the CMB is determined by the density of baryonic matter at that point on the sky during recombination. Dark matter is neutral and therefore cannot experience radiation pressure, so its presence in the universe at that time would increase the size of overdensities in the baryonic matter by condensing while the baryonic matter was still scattering off of photons, thus providing something of a scaffolding for the then emerging cosmic structure.

We can compare the expected distribution of temperature fluctuations of a given angular size for different compositions of the universe between baryonic matter, dark matter, and dark energy by looking at the power spectrum of the CMB, and the latest measurements by the Planck experiment find that the energy density of the universe is approximately 5% standard model particles, 27% dark matter, and 68% dark energy [7,8].

While it is not widely thought to be the case, it is possible that the above evidence for dark matter is compatible with an alternative theory of gravity. However, the discovery of the Bullet Cluster and several other systems of colliding galaxy clusters [9] points strongly towards dark matter composed of massive bodies (as opposed to there being a new theory of gravity at macroscopic scales) as the explanation of the collected evidence. As mass and energy bend spacetime, and light travels along geodesic paths in spacetime, mass bends the path of light around it, and the degree of bending can be used to determine the mass of the object in between the source and observer. Using techniques specific to the weak lensing regime, it has been demonstrated for the bullet cluster that its center of mass and the center of its luminous mass are dramatically misaligned [9]. This is shown in Fig.1.2 This points very strongly to particle dark matter, as it is so far only explained by the presence of a very large amount of mass surrounding both galaxies in the cluster not experiencing any friction due to electromagnetic interactions, and thus continuing on past the center of collision much farther than the luminous matter from either galaxy has.

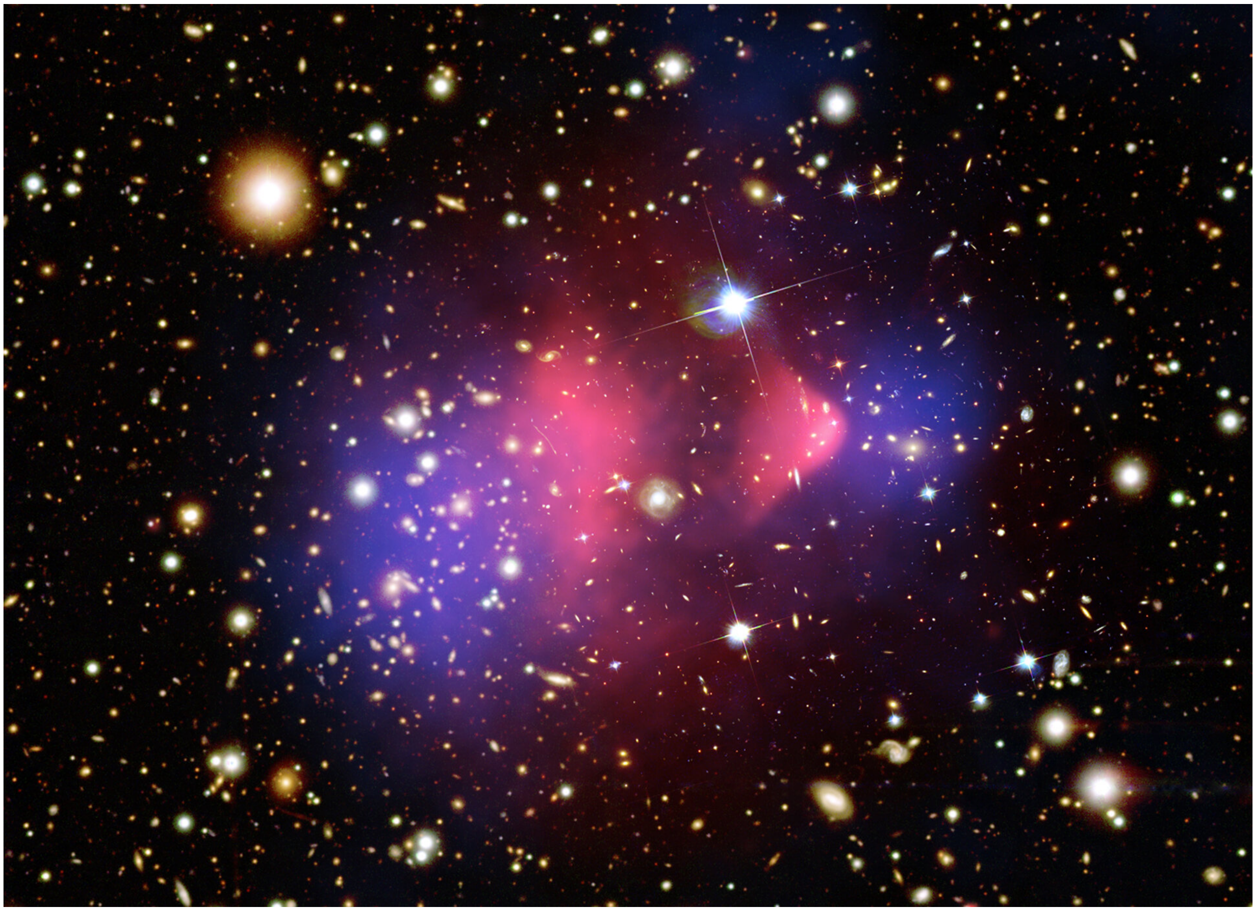

Figure 1.2: The Bullet Cluster [9]. This image is color coded with the red areas being the luminous mass composed of standard model particles and the blue showing where the dark matter is inferred to be from weak lensing.

It is usually assumed that the massive bodies in question are particles, but it is also possible for them to be MACHOs (Massive Compact Halo Objects), although it has been shown that MACHOs composed of baryonic matter cannot make up more than a negligible amount of the missing mass [10].

1.2. Particle Dark Matter

Assuming that the body of evidence we attribute to dark matter is in fact caused by the presence of one or more new species of fundamental particle, it must have a certain set of properties. In particular, any dark matter candidates must be electrically neutral, be experimentally detectable (as otherwise it would not constitute a testable hypothesis), provide the correct relic density, and have mass and interaction cross sections (both self interaction and dm-nucleon interaction) consistent with the constraints obtained from astronomical and cosmological observations and with the constraints obtained from previous generations of direct detection experiments.

Initially it was thought that the most likely candidate for dark matter was WIMPs (Weakly Interacting Massive Particles). [11]. Here weakly interacting specifically refers to an interaction that roughly coincides with the electroweak scale. This was favored for a long time because it has been shown that a particle around 100 GeV which has self interactions of a strength which coincide with the electroweak scale reproduces the observed relic density of dark matter. This is referred to as the WIMP miracle.

However, over the years direct detection experiments have excluded most of the parameter space in which a WIMP is well motivated as the candidate particle for dark matter, and at lower masses there are other more favored candidates like axions or sterile neutrinos. Much of the terminology involved in calculations still refers to WIMPs as the default candidate.

1.3. Detection of Dark Matter

Working under the assumption that dark matter is in fact some heretofore unknown particle or set of particles, there are several ways in which we could detect it and probe its properties. These break down into three broad categories: indirect detection and direct detection, and efforts to produce dark matter in particle colliders. Indirect detection experiments attempt to measure the mass as well as the decay and self-interaction cross sections of dark matter by observing excesses in the energy spectrum of various types of astroparticles (commonly high energy photons like gamma and x rays, as well as different types of cosmic ray particles). The principle is that processes which have dark matter particles as inputs and standard model particles as outputs will create an abundance of certain types of standard model particles relative to what we would estimate based only on known processes.

1.3.1. Direct Detection of Dark matter

Direct detection experiments take advantage of the hypothetical dark matter halo that is centered on our galaxy. We are moving through the galaxy with a velocity of 220 km/s. The effect of this movement relative to the halo is to create a "dark matter wind" from our perspective; a flux of dark matter particles passing through the earth, which changes in magnitude with our yearly change in relative motion to the solar system. Along with the simple fact that we have so far been unable to see dark matter with any part of the electromagnetic spectrum, the evidence collected from observations of the CMB and from the Bullet Cluster point to dark matter being electrically neutral and in general for it to have such low rates of interaction with normal matter that, much like neutrinos, the overwhelming majority of particles in the dark matter wind would pass through the earth without ever actually hitting anything. However, so long as one assumes that the interaction rate between dark matter and standard model particles is not actually zero, as one must if they wish to measure its properties directly, each particle in the dark matter wind still has a small chance of scattering off of an atom and transferring some energy to it. It is these very rare scattering events that direct detection experiments are designed to observe, typically by measuring the energy transferred in the collision.

This energy transfer produces three signals which are measured by direct detection experiments: scintillation light, heat, and ionized charge. The choice of which subset of these signals an experiment measures will determine the materials and detection technology used for the experiment. Most experiments attempt to measure two of the three possible signals because the ratio between them will allow for the identification of different types of particle because different particle types will produce different amounts of each signal, and this is extremely useful for rejecting backgrounds in a rare event search. This is not universal, however. For example when operating in CDMSlite mode SuperCDMS is a phonon only experiment. Some technologies and their associated signals are shown in 1.3.

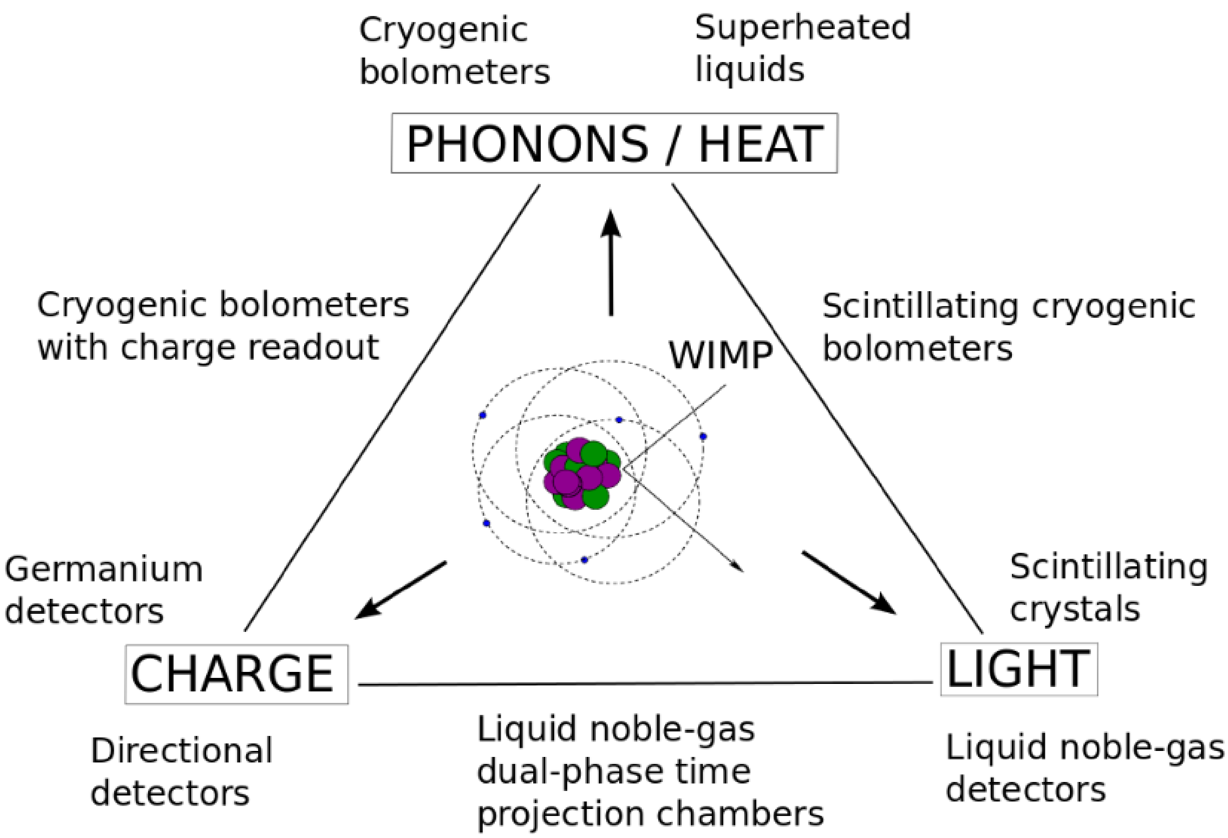

Figure 1.3: A survey of the signals produced by a dark matter event and the technologies used to read them out [12]

Cryogenic bolometer experiments read out heat in the form of quantized vibrations called phonons produced by the initial recoil, and often also read out ionization energy. They usually take the form of a solid crystal, typically of very pure germanium or silicon, held at milikelvin temperatures to reduce thermal vibrations. SuperCDMS, the subject of this work, is a cryogenic bolometer. Some other notable modern cryogenic bolometer experiments are EDELWEISS [13] and CRESST [14]. Cryogenic bolometer experiments have much better sensitivity to low mass (<10 GeV) dark matter than liquid noble experiments, but do not have the advantage of being able to scale easily to high target masses because of the difficulty of fabricating very large crystal detectors. A more comprehensive reviews of the other technologies which are used in direct detection can be found in Ref. [12, 15].

Due to the fact that direct detection experiments are attempting to directly measure the properties of dark matter, they are not dependent on many particular assumptions about the underlying physics of dark matter particles. In particular, the standard assumptions are a non-zero interaction cross section with nucleons (protons and neutrons) and that the interaction between nucleons and dark matter is spin-independent. As a result they can all be fairly neatly compared with each other as they are searching in the same parameter space. Each experiment, failing a discovery, produces what is called an exclusion plot, which maps the lower limit in the mass-interaction cross section parameter space for the area that said experiment would have produced a discovery if dark matter existed with parameters in that area. Below is a collection of the exclusion plots of several notable direct detection experiments.

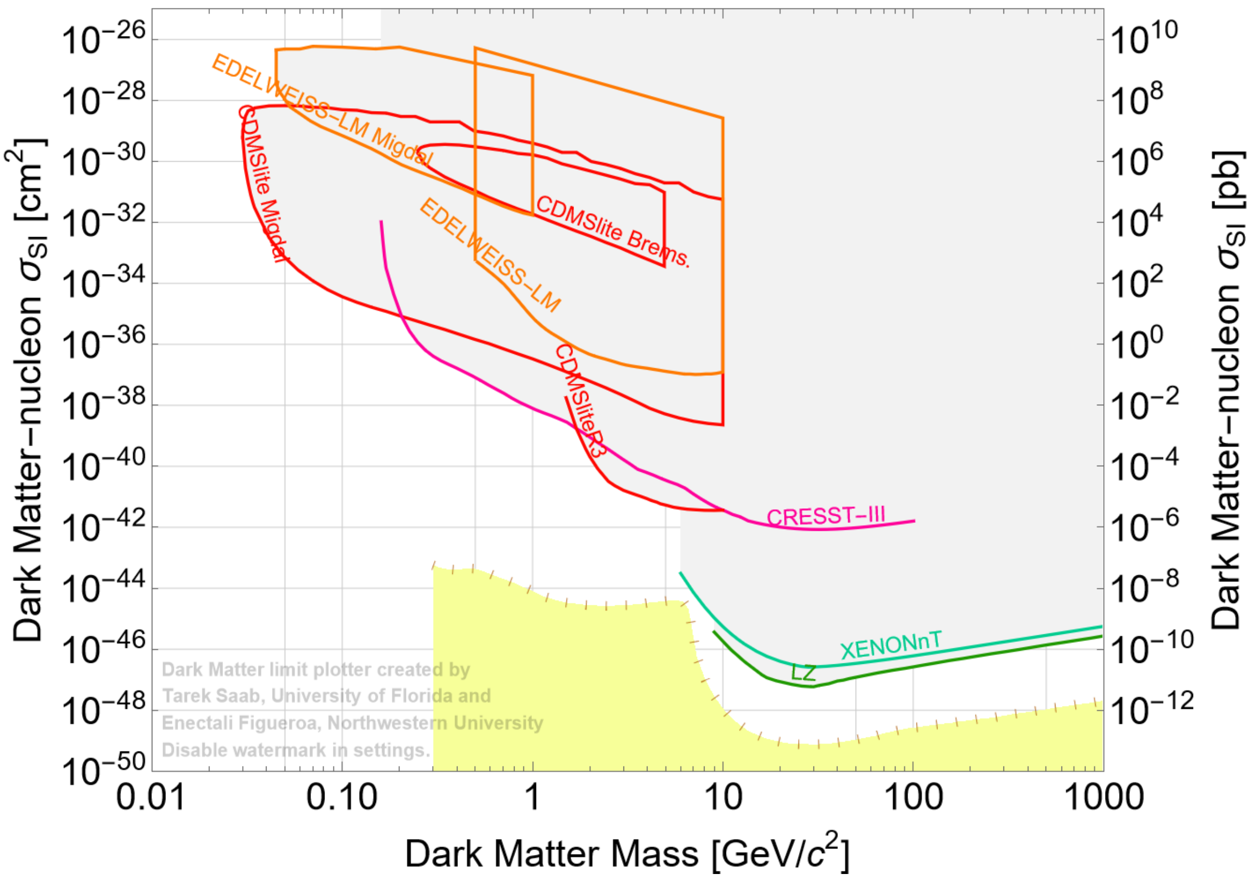

Figure 1.4: The limits of several selected direct detection experiments. The yellow area represents the solar and cosmogenic neutrino background. Below the dashed line the neutrino background becomes comparable to the dark matter signal and severely limits sensitivity, as under current technology there is no way of distinguishing between dark matter scattering events and neutrino scattering events. They greyed out area above each curve is the area excluded by that experiment, as none have so far made a discovery. Some of the above limits have upper bounds as well as lower bounds, and for those limits the area above the upper bound is not excluded.

1.3.2. WIMP Rate

The rate of interaction between dark matter and the detector, called the WIMP rate, is quantified as continuous spectrum measured in keV of energy deposited per kilogram of detector mass per day of exposure time (keV/kg/day) across the range of energies which it is possible to deposit in the detector. This can also be described as the differential of the absolute interaction rate with respect to the energy deposited: $\frac{dR}{dE_r}$. Specifically it is calculated in the following way:

$$\frac{dR}{dE_r} = n_T \frac{\rho_\chi}{m_\chi} \int_{v_{\min}}^{v_{\max}} dv \ v \ f_d(v) \frac{d\sigma_{\chi T}}{dE_r}(E_r, v) \tag{1.1}$$

Where ρ_χ is the dark matter density at the location of the detector, which is assumed to be the same as the local density in our region of the Milky Way (0.3 GeV/cm^3 [16]), m_χ is the mass of the dark matter particle, v is the velocity of the dark matter, $f_d(v)$ is the velocity pdf associated with the dark matter, E_r is the recoil energy, n_T is the number density of atoms in the target material and $\sigma_{\chi T}$ is the interaction cross section between dark matter particles and the atoms in the target material. v_{min} is the minimum kinematically allowed velocity which can produce a nuclear recoil of a given size E_r.

$$v_{min} = \sqrt{\frac{m_T E_r}{2\mu_{\chi T}^2}} \tag{1.2}$$

Where E_r is the recoil energy, $\mu_{\chi T}$ is the reduced mass between the dark matter particle and the target material, and m_T is the mass of the nucleus of an atom of the target material. v_{max} is the maximum possible dark matter velocity relative to us, which is the velocity of earth through the Milky Way (232 km/s) [17] plus the escape velocity of the Milky Way (544 km/s) [18].

$$v_{max} = v_{esc} + v_E \tag{1.3}$$

The vast majority of particles with a higher velocity would have already escaped the galaxy in the billions of years it has existed, and so there are almost no dark matter particles moving faster than that relative to our experiment anywhere in the galaxy.

The differential cross section $\frac{d\sigma}{dE_r}$ incorporates information from nuclear physics to describe how the strength of the dark matter-target nucleus interaction changes with the energy of the collision. Since dark matter is neutral it will not interact electromagnetically with the electrons and so is expected to scatter off of them at a significantly reduced rate compared to dark matter-nucleus scattering. The differential cross section is defined as

$$\frac{d\sigma}{dE_r} = \frac{m_T}{2\mu_{\chi T}^2 v^2}\left[\sigma_{SI}F_{SI}^2 + \sigma_{SD}F_{SD}^2\right] \tag{1.4}$$

Where σ_{SI} is the spin independent cross section between the target atoms and dark matter and F is the nuclear form factor for the target nucleus. The calculated value of F depends on exactly how one chooses to model the nucleus but the most common models are all very close to 1 at the energies involved in this work [19]. The spin independent cross section also incorporates some information from nuclear physics, and can be expanded as follows:

$$\sigma_{SI} = \sigma_{\chi n}\left(\frac{\mu_{\chi T}}{\mu_{\chi n}}A\right)^2 \tag{1.5}$$

Where $\sigma_{\chi n}$ is the interaction cross section between a nucleon and a dark matter particle, $\mu_{\chi n}$ is the reduced mass between a nucleon and a dark matter particle, and A is the atomic mass of the target material. σ_{SD} and F_{SD} encode the equivalent information as their spin-independent counterparts but for interactions whose strength is dependent on the spin of the particles involved. It is assumed that the interactions in this work are purely spin-independent.

1.4. Strong Dark Matter and Windows in Parameter Space

Due to the expectedly very low interaction cross section that dark matter will have with nucleons (protons and neutrons), most analyses of the data collected in these experiments assume that any dark matter reaching the detector has simply not interacted with the earth or atmosphere at all on its way to the experiment. However, since we are assuming non-zero interaction rates between dark matter and normal matter as a necessary prerequisite for our experiments to be justified, the average dark matter particle passing through the earth will have some net amount of interaction with the particles in its path and it will thus lose some energy on its way to the detector. This has a dampening effect on the velocity distribution of dark matter particles that we would expect to see at the detector. This effect is stronger the greater the interaction strength between dark matter and normal matter, and so the net result is that, for any terrestrial, and especially for any underground, experiment there is an upper limit on the cross sections to which it is sensitive for a given hypothetical mass in addition to the lower limit that is achieved without taking this effect into account. Typically the assumption of no pre-detection interaction with the earth begins to break down at $\sim 10^{-30}\text{cm}^2$, which means that the upper limits of most subterranean dark matter experiments will lie in that neigborhood for most masses. For dark matter masses below about 100 MeV [20] there exists a gap between the upper limits of direct detection experiments and the lowest constraints that have been derived from cosmological observations as can be seen in Fig. 1.5.

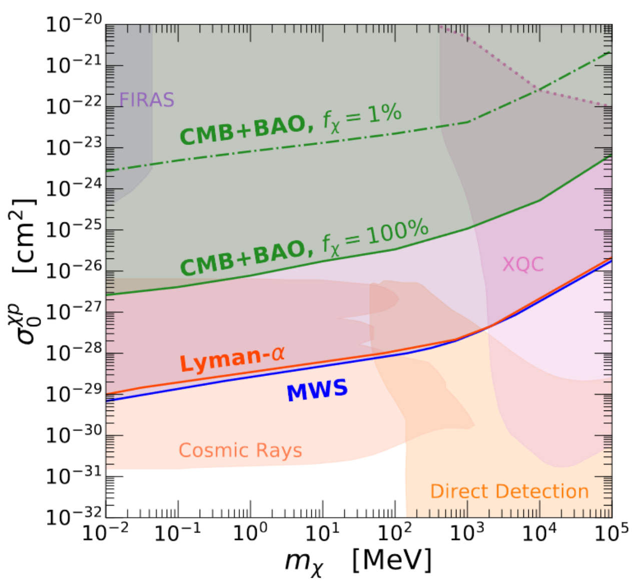

Figure 1.5: Some constraints placed on dark matter properties from cosmological observations [20].

Previously this effect has been applied to data from CDMSlite run 2 and CDMSlite run 3 data to achieve an upper limit for inelastic scattering processes [21]. This work will apply the same technique to CDMSlite run 3 for the case of spin independent elastic scattering.

Chapter 2

The SuperCDMS Experiment

2.1. The CDMS Experiments

The CDMS (Cryogenic Dark Matter Search) program is a series of experiments which aim to directly detect dark matter scattering off germanium and silicon crystals cooled to tens of milikelvin temperatures.

The first experiment in the CDMS program, CDMS I, was conducted in the Stanford Underground Facility (SURF) in Palo Alto, CA from 1998-2002 [22,23]. The second iteration of CDMS, CDMS II began operation in the Soudan mine in Soudan, MN in 2003 [24, 25]. The third and most recent experiment in the program, SuperCDMS Soudan, was an upgrade to CDMS II which deployed new detectors in the existing shielding setup. SuperCDMS Soudan began operation in 2011 [26], and was decomissioned in 2015. The next iteration of the CDMS series of experiments will be SuperCDMS SNOLAB, which will take place in SNOLAB, an underground laboratory in Sudbury, Ontario. Each of the experiments have been underground in increasingly deep locations because this dramatically reduces the cosmic ray and solar radiation flux present at the experiment site relative to the surface. A measure of how protective a facility is against cosmic and solar radiation is the amount of water which would provide the same level of shielding, referred to as the facility's mwe (Meters of Water Equivalent). SURF has 17 mwe of shielding, the Soudan mine has 2090 mwe, and SNOLAB has 6010 mwe. The effect of these increasing levels of shielding can be seen in the muon flux at each site. Muon flux at the SURF site was a fifth of that on the surface, in the Soudan facility it is reduced by a factor of 5×10^4 compared to the surface, and at SNOLAB the muon flux is reduced by 5×10^7 compared to a surface facility.

When a particle scatters off one of the detector crystals two things happen to differing extents depending on the particle type and its energy. The initial impact causes vibrations in the crystal, in much the same way that striking a tuning fork causes it to vibrate. Unlike the vibrations in a tuning fork however, these vibrations are quantized and so they are called phonons. Additionally, the impact will also ionize the specific atom which the particle scattered off of. This ionization produces free electrons, and also a point on the lattice of the crystal which is positively charged relative to those around it, called an electron hole. Electron holes move around on the crystal lattice as if they were particles with charge opposite to that of the electron, and so both free electrons and electron holes can be collected. All of the CDMS experiments prior to the three CDMSlite runs collected both the ionization and phonon signals. The reason the detectors are cooled to extremely low temperatures is so that the phonons, which have very small energy compared to thermal vibrations in the crystal at room temperature, are detectable.

2.2. SuperCDMS Soudan

The Soudan mine is an old iron mine which ceased operation as a mine in 1962. Since the 1980s the lowest level of the mine, which is 2341 feet below the surface, has been converted into the Soudan Underground Laboratory and used for physics experiments due to the very low cosmic ray flux present at the site.

2.2.1. Shielding and Overall Configuration

In addition to being located deep underground, SuperCDMS had many layers of shielding to further protect it from sources of background and of electronic noise, illustrated in Fig 2.1. The outermost layer of shielding was a layer of scintillating panels that served to reject coincidence events caused by muons which passed through the overburden and scattered once off the panels and then once off the detector in quick succession [27]. These panels are referred to as the muon veto. Immediately inside the muon veto was a thick layer of high density polyethelene (HDPE) which lowered the neutron background. This was followed by two layers of lead, the inner of which was made up of ancient lead that had spent an extended period of time on the sea floor and, importantly, had been smelted before the advent of nuclear testing. The layers of lead protect against beta and gamma radiation. The final layer of shielding was a thin layer of HDPE which attenuated neutrons from any decays within the lead layers and absorb neutrons from the cryostat. Inside all of these layers was the cryostat, which was a series of copper cylinders housing the actual detectors [28].

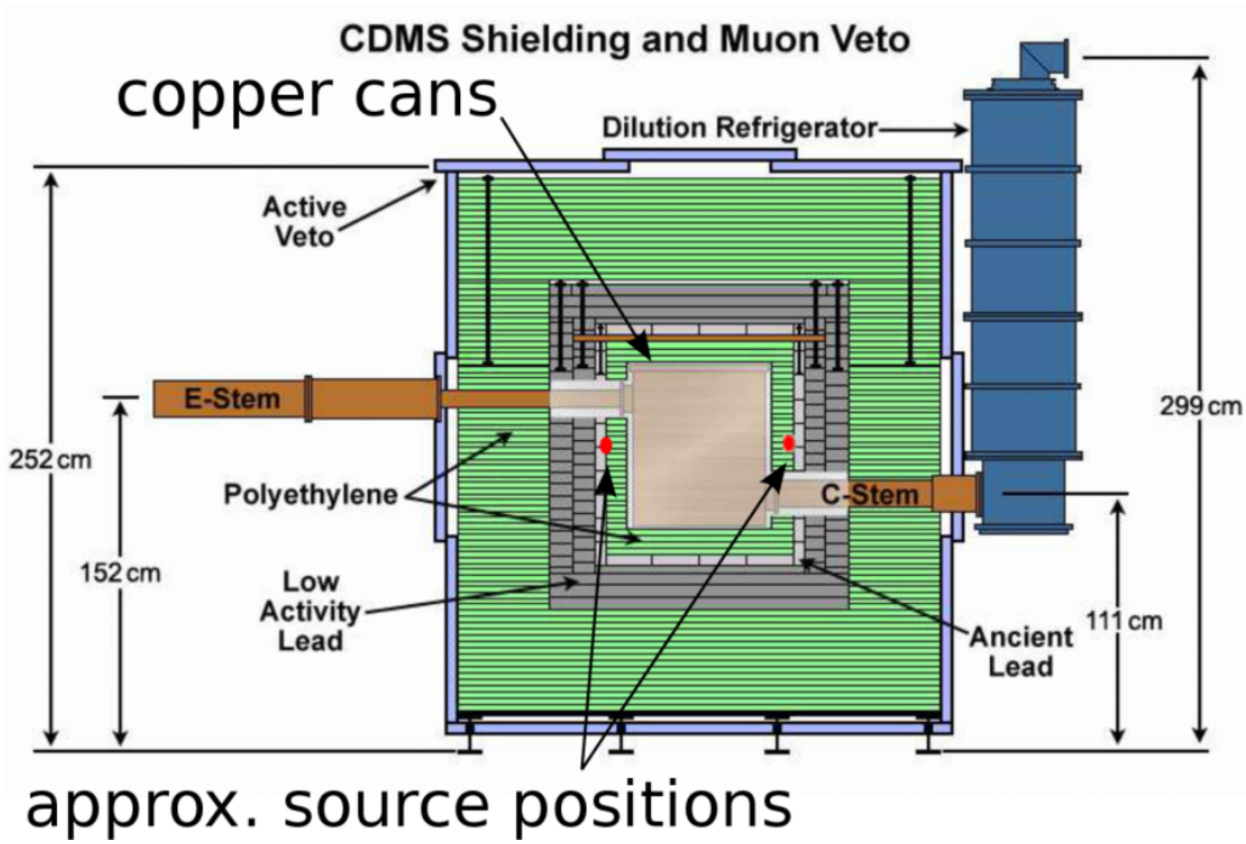

Figure 2.1: Side view of the shielding layers around the Soudan experiment [28]

2.2.2. The iZIP detectors

While SuperCDMS Soudan used the same shielding as CDMS II, it employed 15 new germanium crystal detectors in five towers of three crystals each. The new detectors, called iZIP (interleaved Z-sensitive Ionization and Phonon) detectors, each consisted of a cylindrical germanium crystal 1 inch tall and 3 inches in diameter, weighing 0.6 kg. The detectors were labled according to the tower they were in and their position in that tower. For example, the top detector in the first tower was labeled T1Z1, and the bottom detector in the 5$^{\text{th}}$ tower was labeled T5Z3.

As mentioned in Sec. 2.1, the iZIP detectors collect both ionized charge and phonon energy from each event. This was done by biasing both faces of the crystal to ± 2 V, with the electrodes arranged in such a way that a nearly uniform electric field was created within the volume of the detector. This caused the ionized electrons and and their corresponding electron-holes to drift to opposite faces of the detector. The pulse shape produced when the electrodes on either face collect the free electrons and electron holes was used to determine the vertical position of the event, and the ratio of charge collected by the different electrodes, of which there are many, was used to determine the top-down position of the event.

The iZIP detectors collected the phonons in the following way: after propagating through the crystal phonons would deposit their energy into aluminum fins on the flat face of the crystal, which broke Cooper pairs in the aluminum. The resulting quasiparticles were then collected in tungsten Transition Edge Sensors (TES), causing them to heat up, which changed their resistance sharply, and this functioned as the signal that was ultimately read out, as seen in Fig. 2.2

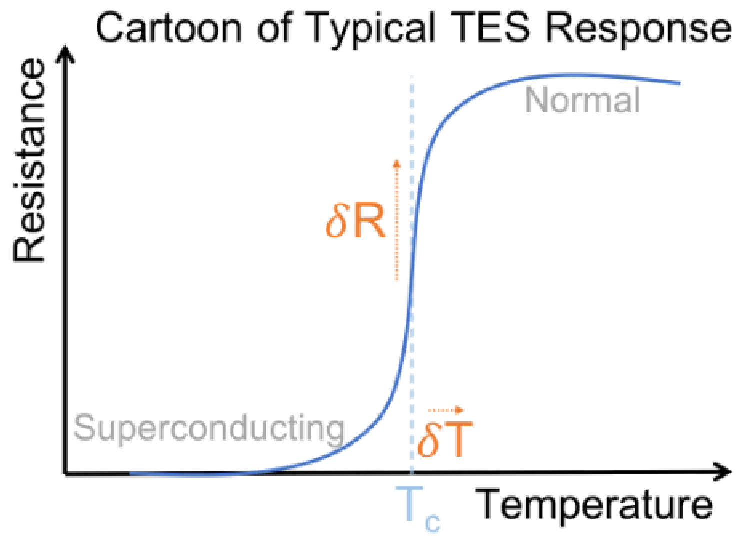

Figure 2.2: A typical resistance curve for a TES. There is a sharp transition after what is known as the critical temperature which allows a very clear readout for when an event happens.

2.2.3. CDMSlite

CDMSlite (Low Ionization Threshold Experiment) is a new mode of operation for the iZIP hardware, intended to give the experiment greater sensitivity to low mass dark matter [29]. In this mode, instead of both faces being biased at ± 2 V, the bottom face is grounded and the top face is biased to +75 V. This much higher bias voltage takes advantage of the Neganov-Trofimov-Luke (NTL) effect, which happens at lower bias voltages but whose strength is proportional to the bias voltage. When electrons drifting through the crystal interact with the crystal lattice they shed energy in the form of phonons, whose energy is proportional to the bias voltage. This means that the total phonon energy collected by the detector for a given scattering event can be described as such:

$$E_t = E_r + N_{eh} eV \tag{2.1}$$

where E_t is the total phonon energy, E_r is the initial recoil energy, N_{eh} is the number of electron-hole pairs created by the ionization event, e is the charge of the electron, and V is the bias voltage. The extra enenrgy collected, $N_{eh}eV$ is referred to as the NTL gain, and greatly lowers the energy threshold necessary for the initial collision to meet before it is detectable, and so increases the experiment's sensitivity to low mass dark matter. Unfortunately, while the electronics can still read out the charge electrodes in CDMSlite mode, the higher voltage required to take advantage of the ampilification of the ionization signal also induced higher electronic noise, which made it impossible to measure the true unamplified charge generated only by the initial scattering. As a result when running in CDMSlite mode we are only capable of using the phonon data for analysis.

The NTL effect amplifies the signal created by the ionization signal in the initial scattering, which is a quantized number of electron-hole (e/h) pairs. The number of pairs created is the ionzation energy divided by the ionization required to ionize one e/h pair:

$$N_{eh} = E_Q/\epsilon$$
$$\epsilon \sim 3 \text{ eV (for germanium)} \tag{2.2}$$

In general for any recoil, the ratio between the ionization energy and the total recoil energy is called the ionization yield:

$$Y = E_Q/E_r \tag{2.3}$$

When the incoming particle is charged and scatters off of the electrons one of the germanium atoms in the detector, called an electron recoil (ER), the yield is one, since all of the energy of the collision is absorbed by the electron and none is absorbed by the nucleus. The number of e/h pair produced in an ER event is

$$N_{er} = E_r/\epsilon \tag{2.4}$$

It is then convenient to define an "energy scale" such that

$$E_r = E_Q = E_{ee}\,[keV_{ee}] \tag{2.5}$$

For a nuclear recoil (NR) event, where the incoming particle scatters off of the nucleus of one of the germanium atoms in the crystal, the energy is partially absorbed by the nucleus and partially by the electrons, so the yield is less than one. Therefore the number of e/h pairs produced in an NR event is

$$N_{nr} = E_r Y(E_r)/\epsilon \tag{2.6}$$

We can define the nuclear recoil energy scale such that

$$E_r = E_{nr}\,[keV_{nr}] \tag{2.7}$$

From this we get equations for the total energy for both NR and ER events:

$$
\begin{aligned}
E_t &= E_{nr}(1 + YeV/\epsilon) \\
E_t &= E_{ee}(1 + eV/\epsilon)
\end{aligned}
\tag{2.8}
$$

Setting these two E_t equal we recover the conversion between the energy scales:

$$
E_{nr} = E_{ee}(1 + eV/\epsilon)/(1 + Y(E_r)eV/\epsilon) \tag{2.9}
$$

Since in general the ionization yield from a nuclear recoil is non constant with the energy of the recoil, a model for Y(E_r) is needed. We use the Lindhard model [30]:

$$
Y(E_{nr}(keV)) = \frac{k \times g(\epsilon)}{1 + k \times g(\epsilon)} \tag{2.10}
$$

Where $g(\epsilon) = 3\epsilon^{.15} + .7\epsilon^{.6} + \epsilon$, $\epsilon = 11.5E_{nr}Z^{7/3}$, Z is the atomic number of the target material, and k is measured to be .157±.05 for germanium [31].

This analysis focuses specifically on the third data taking run using the CDMSlite mode, CDMSlite run 3. As was the case with the previous runs only one detector was used. Run 3 used T2Z1 instead of T5Z2, which was the detector used in the previous two runs. After all data quality cuts had been made, this run produced a total of 36.92 kg-d of exposure at an energy threshold of 70 eV(keV_{nr}).

Chapter 3

CDMSlite run 3 Analysis

3.1. Data

3.1.1. Data used in this analysis

There were three types of data sets used in the analysis of CDMSlite run 3: the barium and californium calibration data as well as the low background data which was used to search for dark matter. The calibration data was used for calibrating the energy scale, calculating the cut efficiency, and measuring the resolution. The Ba-133 source is a high-rate gamma-emitter and was used to understand detector response to electron recoils. The Cf-252 source is a neutron-emitter and was used to understand detector response to nuclear recoils.

The barium spectrum has one very large peak at 356 keV and a series of smaller peaks at 276 keV, 303 keV, and 383 keV. These features were used for energy calibration when the detectors were run in iZIP mode because the high energy gammas which produce them penetrate through the inner layers of shielding and throughout the detector crystals, so they are evenly distributed throughout the bulk of the crystal. In CDMSlite mode the detector response saturates around 30 keV so the barium spectrum cannot be used for calibration, but its features are still useful for efficiency calculations.

When the californium source is exposed to the detector, the stable germanium atoms can capture neutrons emitted by the californium and become heavier unstable isotopes. There two primary decay channels which produce a spectrum in the detector. The first and most simple is when Ge-73 decays via a 66.7 keV gamma ray [32]. The 2$^{\text{nd}}$ and more complicated channel is that Ge-71 can capture an electron, which results in the release of gamma rays and Auger electrons. When this happens the total energy from the decay is determined by the binding energy of the shell that captured the electron. The inner K-shell, L-shell, and M-shells have an 87.57%, 10.53%, and 1.78% chance respectively of capturing an electron and result in 10.37 keV, 1.3 keV, and 160 eV emissions respectively [33].

Part way through the data taking period, adjustments were made which stabilized the bias voltage on the detector at 75 V when previously it had drifted between 50 V and 75 V, necessitating a correction to the energy scale in the analysis of the data from the earlier period. Once the detector had stabilized at 75 V its phonon noise performance worsened. These adjustments created two distinct operating conditions: one with reduced phonon noise and an unstable detector bias voltage and another with stable detector bias voltage and increased phonon noise. Thus the low background data was split into two pieces which were analyzed separately, called R3a and R3b.

3.1.2. Overview of data quality cuts

The data contains several types of undesirable events which need to be removed before an analysis can be properly performed: events which correspond to low frequency noise (LFN) triggering the detector, events which are poorly reconstructed and thus cannot be used, events which took place during periods of anomalous detector behavior, and events which correspond to a single particle scattering multiple times off the experiment. The cuts which reject all data from periods of anomalous behavior are called livetime cuts, because they act to reduce the total exposure of the experiment rather than removing individual events. Cuts which remove individual undesirable events are reffered to as quality cuts.

Anomalous detector behavior includes when there are multiple events pulses in a single pulse window, events which did not have a GPS time recorded or where there was a significant difference between recorded event time and GPS time, periods where the detector was not biased to the correct voltage, events which had an elevated amount of noise in their prepulse, "glitch" pulses which have pulse shapes which are unphysically fast for a real physics event and are caused by electronics noise, and periods of time when the Fermilab neutrino beam was running. These events were all removed because they were either clearly not dark matter events, they happened during a period of time where the detector was operating with increased noise, or when the detector was in a significantly increased background (e.g when the Fermilab neutrino beam was on).

Dark matter interacts very weakly with normal matter so the probability of a dark matter particle scattering off of the crystal more than once as it passes through the earth is extremely small. Therefore any pair of events that are sufficiently close together in time are assumed to be the same particle scattering multiple times in the detector, and is therefore assumed not to be a dark matter event. Specifically an event in one of the other detector crystals occurs within a -200 μs to $+100$ μs window relative to an event in the CDMSlite crystal, or if an event in the muon veto surrounding the detector occurs in a -185 μs to $+20$ μs window relative to an event in the CDMSlite crystal, the pair of events are tagged as multiple scattering event and removed from the data.

Biasing the detector on only one face means that the voltage inside it is not uniform everywhere when running in CDMSlite mode, as shown in Fig. 3.1. Events which occur more than $\sim$ 16 mm from the center line of the crystal do not always experience the full bias voltage. This leads to them not experience the full NTL amplification that events in the main bulk of the detector do. Because we cannot precisely reconstruct the position of an event, we can't correct for this by using the position to know what potential the charge is exposed to, so if these events are not removed from the data set they will have incorrectly reduced reconstructed energies. However, because we cannot precisely reconstruct position we cannot remove these events by just cutting all events with a radial distance from the center greater than 16 mm, so some other strategy must be employed.

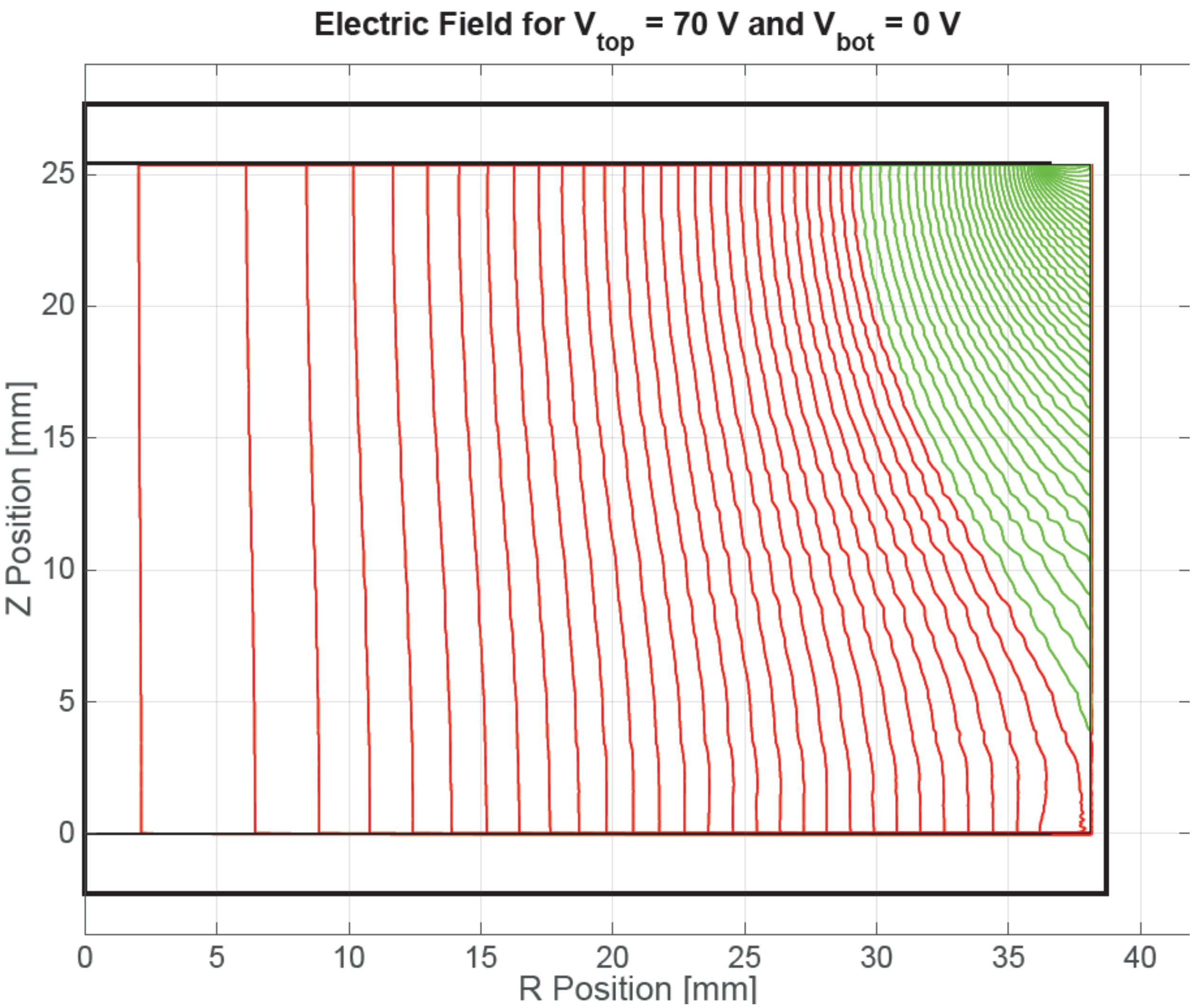

Figure 3.1: The electric field configuration for the detector. As this plot shows, for high radius events the E-field is non-uniform. Green regions are areas where the experienced bias voltage is less than that in the bulk; in this case 70 V [33]

To solve this problem a two-template optimal filter was developed which fits a "slow" template to the phonon pulse to extract information about the total event energy. The slow template is subtracted from the pulse and the remaining signal is fit with a "fast" template which is much narrower in time than the slow template. The fast template is sensitive to the event position, since the phonon channel closest to the event will read a faster pulse.

The ratio of the amplitudes from the two fits is used to define a radial parameter ξ which is correlated with the radius and can be can be used to discriminate between events with a high radius and events with a low radius in order to remove events near the side wall of the crystal.

Because we are performing a profile likelihood analysis, all backgrounds in the data need to be modeled so they can be incorporated into the likelihood function. Low frequency noise (LFN) produced by vibrational sources, however, is not a modelable background and has a significant enough overlap with the bandwidth of the real signal pulses that if not removed it could be mistaken for signal events later on in the analysis. Therefore a cut had to be developed which left fewer than one expected LFN event in the data. For this, two boosted decision tree based cuts were tuned using the bifurcated analysis technique [34].

3.2. Background Modeling

A prerequisite for calculating the profile likelihood limit are the probability distribution functions (pdfs) for each source that contributes to the total background. For this analysis neutron activation by the californium source, cosmogenic activation of the crystal, Compton scattering from radioactive materials within the experiment, and Pb-210 contamination of the experiment were all modeled independently and make up the total background which has been accounted for.

The spectrum resulting from Ge-71 decay due to californium exposure is modeled as a series of Gaussian distributions with one for each peak. The amplitude of the L-shell and M-shell peaks are set relative to the K-shell peak, so there is only one overall normalization parameter in the likelihood function for the Ge-71 background.

The term cosmogenic activation refers to the creation of radioisotopes in the detector crystal when it is hit by cosmic rays. This happens when the detector is still above ground while it is being fabricated and transported to the experiment site. Of the radioisotopes which are created in the crystal while it is above ground, tritium dominates the resulting spectrum with smaller contributions from Ga-68, Zn-65, and Fe-55 also being incorporated into the model for this background. For this analysis the threshold for inclusion in the background model was that the radioisotope in question must have a half-life such that it will not decay before data taking begins and that it contributes at least one expected event over the course of data taking.

The decay of radioisotopes near but not within the detector can contribute to the low energy backgrounds via Compton scattering which conveys only a fraction of the photon energy to the detector (i.e cases where the photon loses energy by scattering multiple times off of parts of the environment like the copper housing before it hits the detector crystal or cases of low angle scattering). This results in a spectrum which is roughly flat in the analysis region, but which has steps at low energy corresponding to the points below which the scattered photon cannot overcome the binding energy of the electron shell [35].

At lower energies the spectra for the tritium and Compton pieces of the background are both nearly flat and are degenerate with each other, which creates a problem when trying to create best fit models for the background components because they are not easily distinguished in this range. This is solved by extending the analysis to higher energy ranges above the endpoint of the tritium spectrum, which has an endpoint of 18.6 keV. Above these energies the dominant background is the Compton model and similarly above 10.37 keV (the Ge-71 K-shell energy), the dominant non-Compton background is the tritium. In this way the degeneracy between the tritium and Compton backgrounds was broken and best fit normalizations were obtained.

3.2.1. Surface background models

The backgrounds previously discussed are all distributed uniformly throughout the crystal, which allows for the efficiency of the cuts developed for a uniformly distributed WIMP signal to be applied to them. This makes it possible to model these backgrounds as analytic functions, as has been described. This property does not hold true for the background which comes from the decay of radon daughters on and in the surface of the detector and the surface of the copper housing. In order to understand this background Pb-214 contamination mimicking that found in the actual detector was added to a simulation of the detector in GEANT4 [36–38] and a simulated voltage map inside the detector was used to model the detector response to the subsequent decays. This method brings with it two primary systematic uncertainties which need to be accounted for: variability in the voltage map relative to the true voltage due to it not having incorporated the fields from the adjacent detector crystals, and uncertainty in the physical location of a voltage-based cut.

The results of the simulation were normalized using the results of alpha rate studies done with the detectors in iZIP mode. This was done because iZIP data contains much more information about the position of an event than data collected in CDMSlite mode, which allowed the alphas to be attributed to one of the sources mentioned above. This is useful because the alphas are products from the decay of radon daughters which are easily identifiable as such, so mapping the the alpha rate is a proxy for the rate of 20 keV nuclear recoils resulting from the decay of radon daughters which would not otherwise be able to be distinguished as background events. Using this data, the normalization for each source was arrived at in the following manner: Because the detector is at the top of the tower, its bottom face is directly adjacent to the top face of another detector, so the rate from the bottom face is divided by two and then scaled by the ratio of the areas of the bottom face and vertical face of the germanium to get the number of events coming from the side wall of the germanium. Subtracting the number for the bottom face from the number for the top face gives the rate of events originating in the top lid of the housing and subtracting the number of side wall events from the number of events which occurred in the side wall gives us the number of events which came from the copper housing which faces the side of the germanium.

The smoothed models and systematic errors are shown in Fig 3.2.

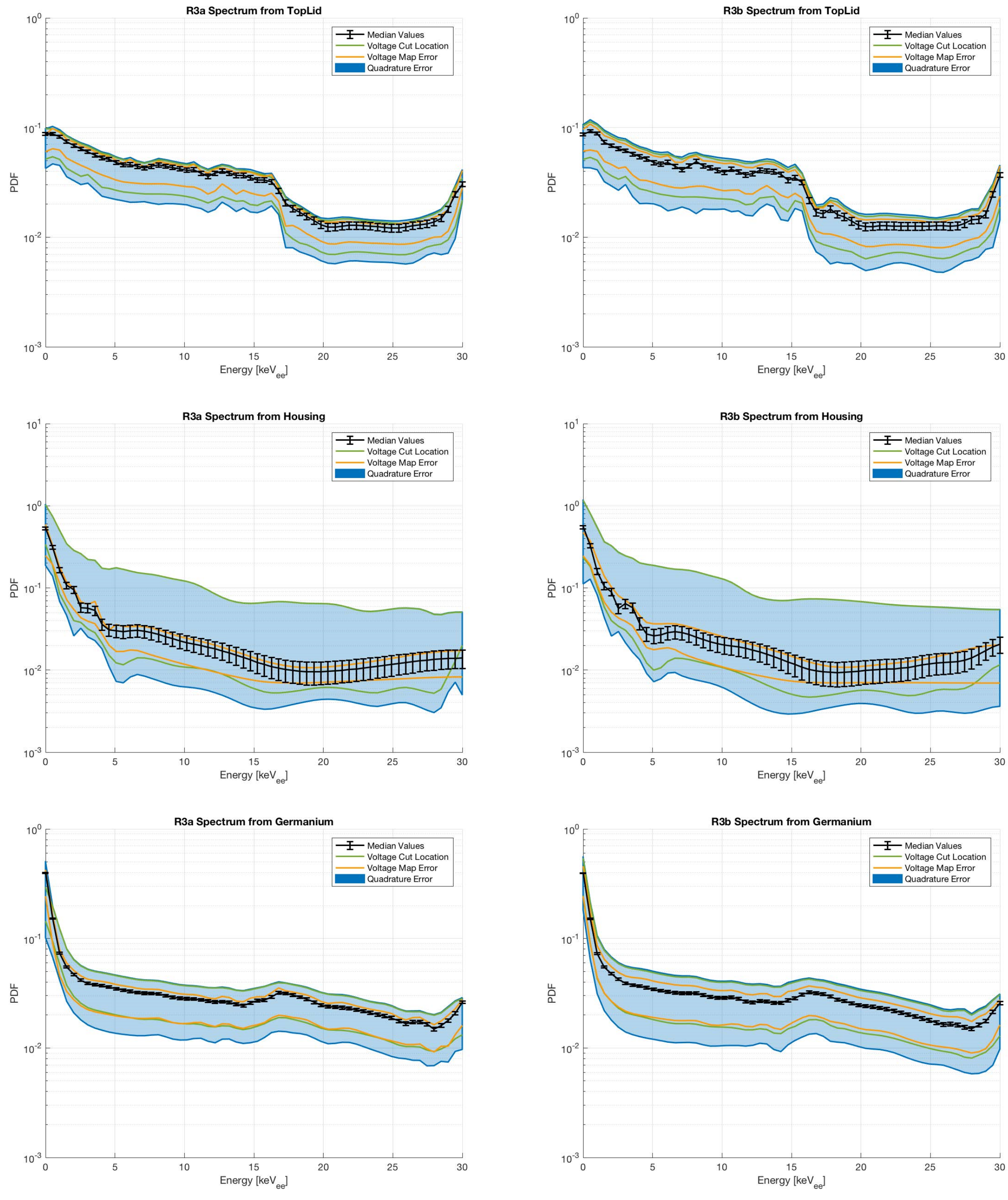

Figure 3.2: Surface backgrounds for all three sources from R3a (left) and R3b (right). The orange curves represent the systematic error on the voltage map used in the simulation and the green lines represent the systematic error of the voltage cut location. The black median curve has been scaled to a pdf with unit area and is shown with statistical error bars. The green and orange lines have been scaled to maintain the ratio with the black curve, and the blue curves are the quadrature sum of the statistical and systematic errors.

For the 0-25 keV range in this analysis, this process gives $N_{Top\ Lid} = 93.6 \pm 9.8$ events, $N_{Sidewall\ Housing} = 13.2 \pm 0.8$ events, and $N_{Germanium\ iZIP} = 13.9 \pm 3.5$ events. With correlation coefficients $\rho_{Tl,SH}$ = -.225, $\rho_{SH,GZ}$ = -.3395, $\rho_{GZ,TL}$ = -.18. Adjusting these numbers according to the efficiency of the cuts used in the simulation gives $N_{Top\ Lid} = 158.4 \pm 16.6$ events, $N_{Sidewall\ Housing} = 22.3 \pm 1.4$ events, and $N_{Germanium\ iZIP} = 23.5 \pm 5.9$ events. The resulting covariance matrix is:

$$C_N = \begin{bmatrix} 274.96 & -5.05 & -17.68 \\ -5.05 & 1.83 & -2.72 \\ -17.68 & -2.72 & 35.07 \end{bmatrix} \tag{3.1}$$

3.2.2. Background Morphing

Because the uncertainty band does not have the same shape as the median curve, the shape of the spectrum and its normalization are correlated, and so the background shape and size cannot be determined independently. This must be accounted for in the likelihood function. This is done via a "morphing" parameter m, which is allowed to float in the likelihood function, implemented in the following manner:

$$\rho(E,m) = \begin{cases} \rho_{med}(E) + m(\rho_{upper}(E) - \rho_{med}(E)) & for\ m > 0 \\ \rho_{med}(E) + m(\rho_{med}(E) - \rho_{lower}(E)) & for\ m < 0 \end{cases} \tag{3.2}$$

Where the pdfs in Fig 3.2 have been scaled to be event densities by multiplying them by the predicted normalization. The median curve is ρ_{med}, ρ_{upper} is the upper bound of the 1σ uncertainty band, and ρ_{lower} is the lower bound of the 1σ uncertainty band.

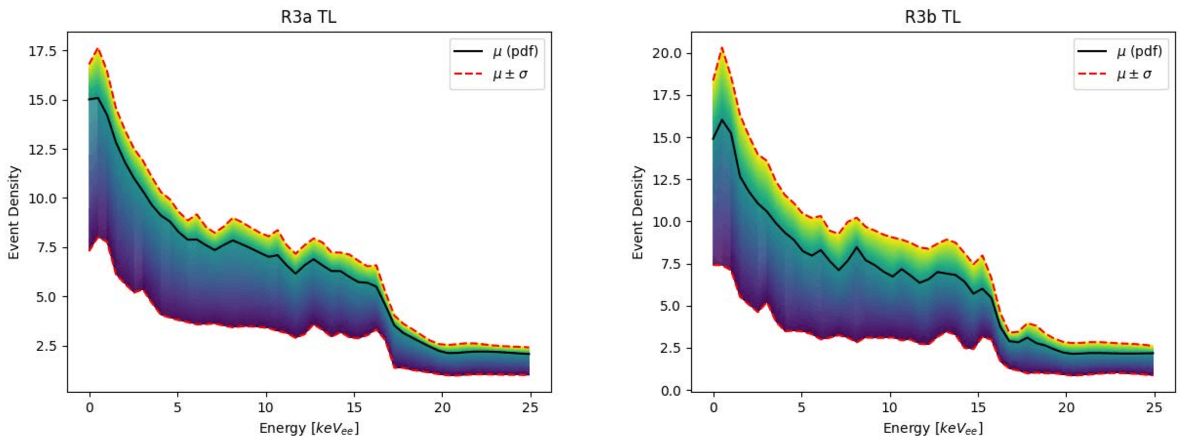

Figure 3.3: Morphing the event density model of surface events from the copper top lid for R3a (left) and R3b (right)

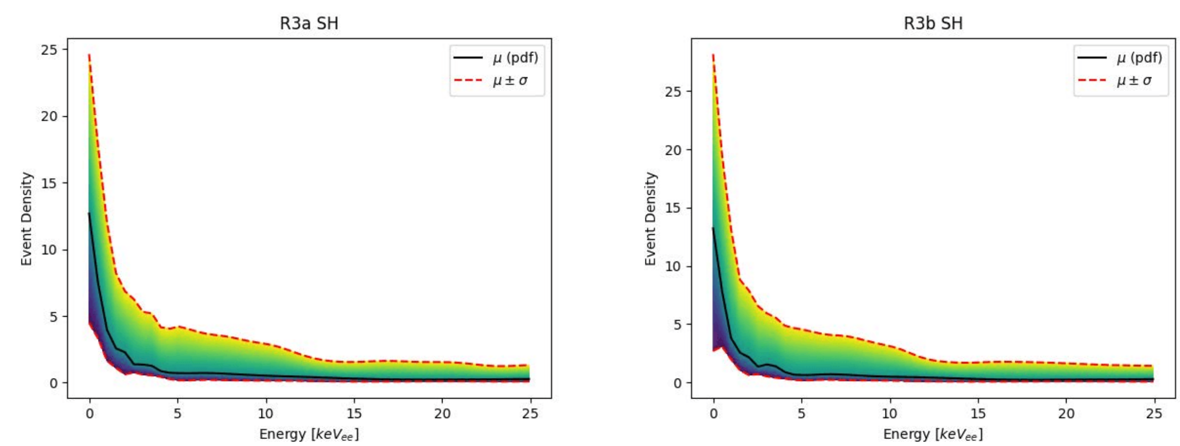

Figure 3.4: Morphing the event density model of surface events from the copper sidewall housing for R3a (left) and R3b (right)

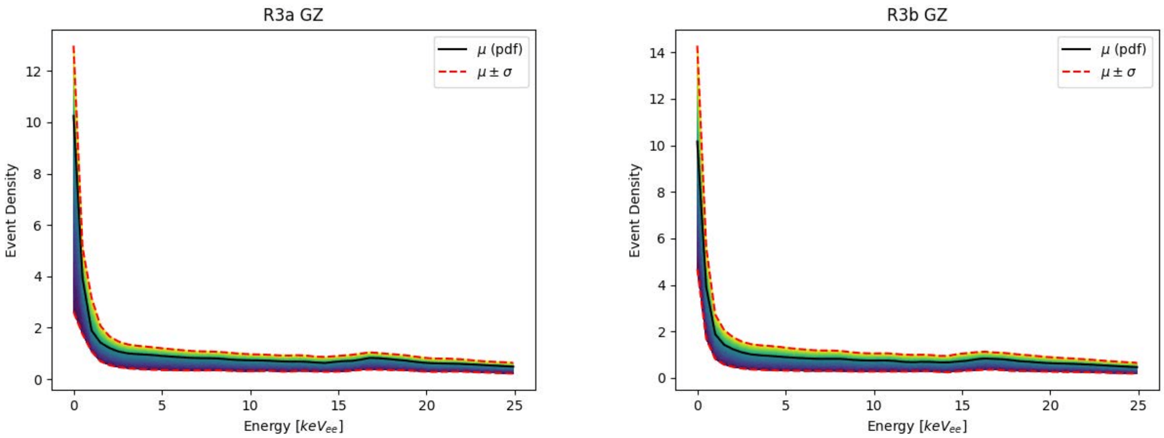

Figure 3.5: Morphing the event density model of surface events from the germanium crystal for R3a (left) and R3b (right)

The above figures were generated by linearly sampling the morphing parameter for each source between -1 and 1, but the morphing parameter for each source will be constrained with a Gaussian distribution with a mean $\mu = 0$ and standard deviation $\sigma = 1$. This will penalize the likelihood function from moving away from the median value of the morphing parameter. In order to incorporate this into the likelihood function we need to translate the uncertainty in the morphing parameters into uncertainty on the normalization of each surface background. To do this, the value for each of the three morphing parameters is assigned by randomly sampling a one dimensional Gaussian. Each of the surface backgrounds is then morphed using its corresponding value of m as described in Eq. 3.2. The total number of events for each surface background is calculated using Eq. 3.3, and the histograms showing the number of events for each model are shown in Fig. 3.6

$$N_x = \int \rho_x(E) dE \tag{3.3}$$

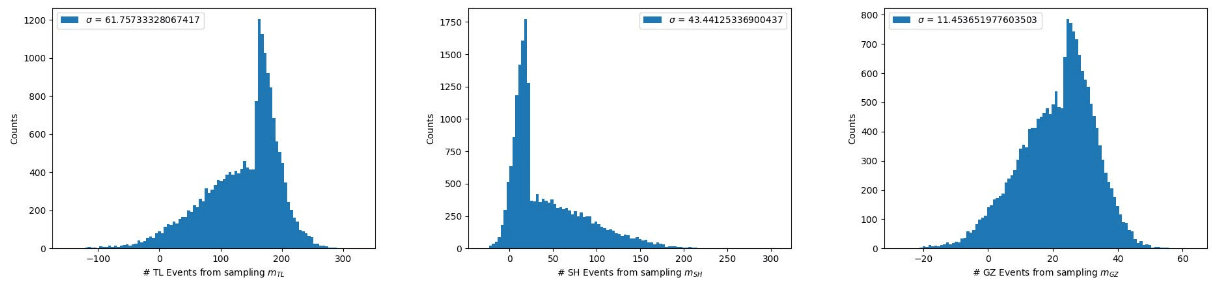

Figure 3.6: Histograms of the number of events from Gaussian sampling of the top lid morphing parameter (left), sidewall morphing parameter (center) and germanium morphing parameter (right)

The morphing parameter uncertainty is:

$$C_m = \begin{bmatrix} 3042.79 & 2044.55 & 621.58 \\ 2044.55 & 1870.56 & 413.8 \\ 621.58 & 413.8 & 116.35 \end{bmatrix} \tag{3.4}$$

Combining this with Eq. 3.1, we get the total covariance matrix on the number of events from each source:

$$V = \begin{bmatrix} 3677.75 & 2039.50 & 603.91 \\ 2039.50 & 1872.39 & 411.08 \\ 603.91 & 411.08 & 151.42 \end{bmatrix} \tag{3.5}$$

The final step is then to turn the covariance in the surface background normalization into covariance on the values of the three m parameters since those are included in the likelihood function. Plotting the relationship between the number of events and the morphing parameter, as shown in Fig. 3.7, allows us to convert the uncertainty on the number of events from each source to the uncertainty on the corresponding morphing parameter. Using this equation we arrive at the matrix M which contains the total covariance of the three morphing parameters:

$$M_{ij} = \sum_{k,l}^{3} \frac{\partial m_i}{\partial N_k} \frac{\partial m_j}{\partial N_l} \quad |_{x=\mu} \times V_{kl} \tag{3.6}$$

$$M = \begin{bmatrix} 1.08 & 0.86 & 0.92 \\ 0.86 & 1.15 & 0.90 \\ 0.92 & 0.90 & 1.19 \end{bmatrix} \tag{3.7}$$

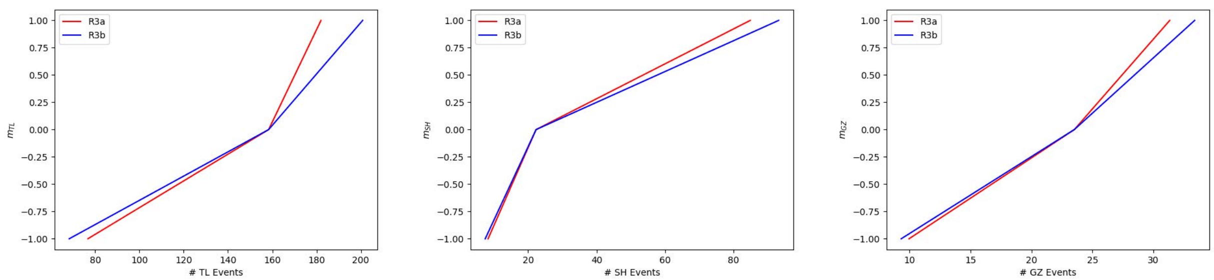

Figure 3.7: Plots of the number of total events from top lid (left), sidewall (center) and germanium (right) as a function of their respective morphing parameters

3.3. Efficiency

The efficiency of the quality and fiducial volume cuts discussed in section 3.1.2 is calculated by simulating raw pulses and processing them as normal, then applying the cuts to that data and calculating the passage fraction as a function of energy. This will produce a total efficiency curve for all the cuts together over the energy range of the analysis.

To obtain a final spectrum matching the data, all of the models are multiplied by the efficiency of the set of cuts used. Due to the inherent uncertainty in the efficiency, the efficiency curve was included in the likelihood function which required it to be parameterized by a nuisance parameter. This was done in the same way as the previous section, with a morphing parameter. The resulting efficiency curve, shown morphed between $m = -1$ and $m = 1$, is shown in Fig. 3.8.

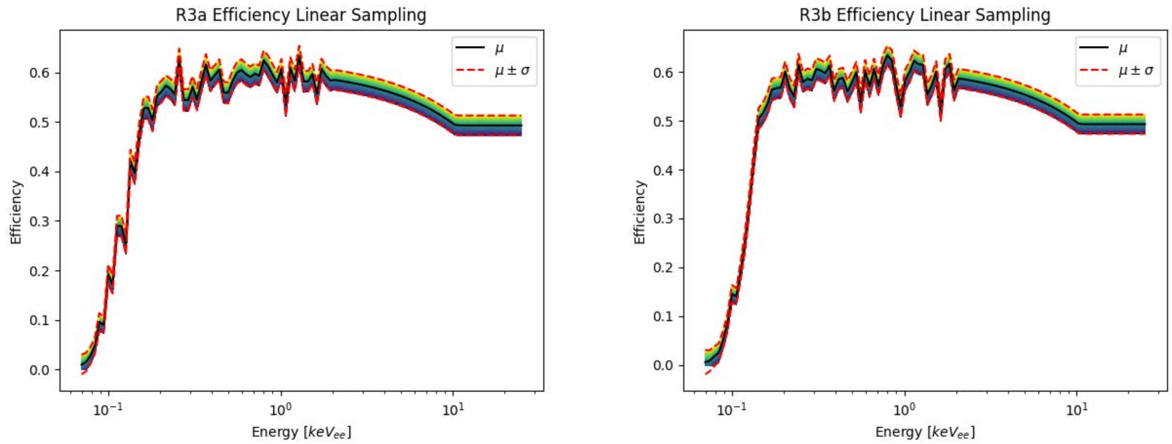

Figure 3.8: The efficiency curves for R3a (left) and R3b (right) morphed between$m = -1$ and $m = 1$

3.4. Resolution

Finally, in order to properly correspond to the data collected by the experiment the background and signal models are "smeared" (convolved) with the resolution of the detector, which is a function and non-uniform across its entire sensitive range. The functional form of the resolution, as a function of energy is:

$$\sigma^2(E) = A + BE + CE^2 \tag{3.8}$$

Where σ is the resolution, A is noise added to every event from the readout electronics and is independent of energy, B is an intrinsic variance due to the Fano factor of the material and is directly proportional to the energy, and C is a corrective constant which accounts for mis-estimation of the energy due to the optimum filter templates having a constant pulse shape and real pulses varying somewhat as functions of energy and position.

The resolution at 0 keV, as well as at the germanium activation peaks at 10.37 keV, 1.3 keV, and 160 eV were measured. These points were then then plotted and then used generate a continuous best fit model of the resolution, shown in Fig. 3.9 and summarized in Table 3.1.

From this we can get the covariance matrices for each sub run are:

$$R_{R3a} = \begin{bmatrix} 1.6\times10^{-9} & -3.428\times10^{-11} & 3.066\times10^{-10} \\ -3.428\times10^{-11} & 1.475\times10^{-8} & -1.467\times10^{-7} \\ 3.066\times10^{-10} & -1.467\times10^{-7} & 1.625\times10^{-6} \end{bmatrix} \tag{3.9}$$

$$R_{R3b} = \begin{bmatrix} 1.6\times10^{-9} & -4.233\times10^{-11} & 3.393\times10^{-10} \\ -4.233\times10^{-11} & 1.473\times10^{-8} & -1.319\times10^{-7} \\ 3.393\times10^{-10} & -1.319\times10^{-7} & 1.316\times10^{-6} \end{bmatrix} \tag{3.10}$$

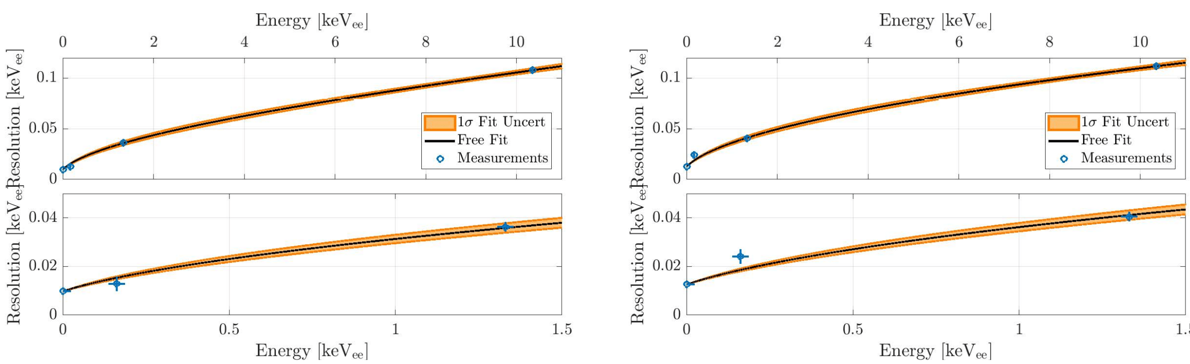

Figure 3.9: The blue points are the measured resolutions of the baseline noise and germanium activation peaks. The black curve is the best fit of the resolution model, and the orange band is the uncertainty of that fit. The top plot shows the measured peaks up to 11 keV, while the lower plot is zoomed in below 1.5 keV. The left figure is the resolution curve for R3a, an the right figure is the resolution curve for R3b

Peak	Energy[keV$_{ee}$]	Resolution[eV$_{ee}$]	Res.Err.[eV$_{ee}$]
R3a Baseline	0	8.87	.04
R3b Baseline	0	12.67	.04
M-Shell	.36	13.9	2
L-Shell	1.3	36.3	2
K-Shell	10.37	108	2

Run	A[eV]	B[eV]	C
R3a Baseline	9.87±0.04	.87±0.12	$(4.94\pm1.27)\times10^{-3}$
R3b Baseline	12.7±0.04	.80±0.12	$(5.49\pm1.15)\times10^{-3}$

Run	ρ_{AB}	ρ_{BC}	ρ_{CA}
R3a Baseline	-0.0071	-0.9474	0.0060
R3b Baseline	-0.0087	-0.9474	0.0074

Table 3.1: The measured resolutions of known features in the data (top), resolution model parameters from fitting to the measured widths (middle), and correlations between the model parameters (bottom).

Chapter 4

Overburden

4.1. Theory

The experiment takes place underground, so any dark matter which scatters off of the detector and produces an event signal must pass through the Earth's crust and atmosphere. Since any dark matter which can scatter off the detector has a non-zero interaction cross section with nucleons, some scattering can occur between outer space and the detector, and cause the dark matter particles to slow down and lose some energy. For high cross sections around 10^{-30} cm^2 this results in a serious reduction and then eventually total loss of experiment's sensitivity to dark matter candidates in that region of parameter space. The following is an explanation of the analytic method laid out in method b in [39] by Emken and Kouvaris to account for the changes in the dark matter velocity distribution which result from this pre detection scattering. It should be noted that this method will, when carried through the profile likelihood analysis discussed in the next chapter, result in a conservative upper bound on the sensitivity, and it would be possible to extend that bound by using Monte Carlo simulations instead of accounting for the average effect analytically.

The differential event rate for a generic direct detection experiment is:

$$\frac{dR}{dE_R} = \sum_i n_i \frac{\rho_\chi}{m_\chi} \int_{v_{\min}}^{v_{\max}} dv \ v \ f_d(v) \frac{d\sigma_{\chi i}}{dE_R}(E_R, v) \tag{4.1}$$

Where ρ_χ is the dark matter density at the location of the detector, which is assumed to be the same as the density in space, m_χ is the mass of the dark matter particle, v is the velocity of the dark matter, $f_d(v)$ is the velocity pdf associated with the dark matter, E_R is the recoil energy, n_i is the number density of a given nuclear species i in the target material and $\sigma_{\chi i}$ is the dark matter cross section with that species. The variable i indexes all the different nuclear species in the target. For this analysis there is only one nuclear species in the target: Ge-70. Where v_{min} and v_{max} are defined identically to Sec. 1.3.2.

Emken and Kovaris adjust the velocity of a single particle passing through one layer of homogeneous material:

$$v_\chi^{fin}(d) = v_\chi^{initial} \exp[-\frac{\rho\sigma_{\chi n}}{m_\chi \mu_{\chi n}^2}(\sum_i \frac{f_i \mu_{\chi i}^4 A_i^2}{m_i^2})d] \tag{4.2}$$

$$v_\chi^{fin}(d) = v_\chi^{initial} \exp[-\Delta d] \tag{4.3}$$

Where d is the path length through the layer, ρ is the mass density of the layer, $\sigma_{\chi n}$ is the dark matter-nucleon scattering cross section, $\mu_{\chi n}$ is the reduced mass between a dark matter particle and a nucleon, f_i is the mass fraction for a given nuclear species in the layer, $\mu_{\chi i}$ is the reduced mass between a dark matter particle and a given nuclear species, m_i is the mass of said nuclear species, m_χ is the mass of a dark matter particle, and A_i is the mass number of the nuclear species. The variable i indexes all of the nuclear species that compose the material of that layer.

This results in the overall velocity distribution being modified in the following way:

$$f_d\left(v_\chi^{fin}\right) = \exp[2\Delta d] f\left(\exp[\Delta d]\left(v_\chi^{fin}\right)\right) \tag{4.4}$$

This results in the velocity distribution becoming more sharply peaked and having its peak moved towards 0 m/s as the value of d goes to infinity, as can be seen in Fig. 4.1:

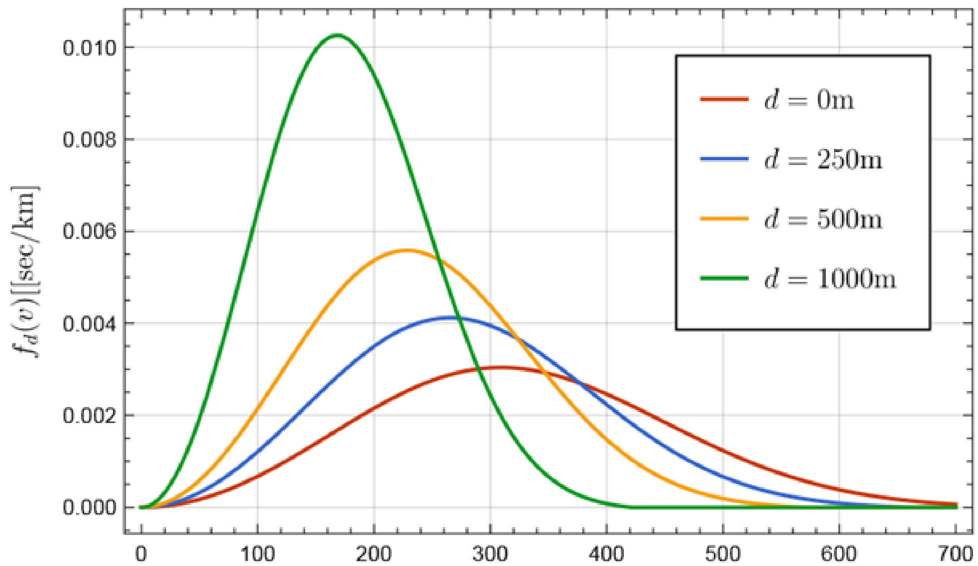

Figure 4.1: The effects of passing through a single layer on the velocity distribution for $m_\chi = 1$ GeV, $\sigma_{\chi n} = 10^{-30}$ cm^2 [39]

The new expected differential event rate is then:

$$\frac{dR}{dE_R} = n_T \frac{\rho_\chi}{m_\chi} \int_{v_{\min}}^{v_{\max}} dv\ v\ \exp[2\Delta d] f\left(\exp[\Delta d]\left(v_\chi^{fin}\right)\right) \frac{d\sigma_{\chi i}}{dE_R}(E_R, v) \tag{4.5}$$

4.1.1. Practical Considerations

Unfortunately, much like a cow, the Earth is not a homogeneous sphere, so the above calculation must be performed consecutively for each different layer of the Earth that the dark matter passes through on its way to the detector. Our calculations included the atmosphere, the ocean, the mantle, the outer core, and the inner core as distinct homogeneous layers in addition to incorporating a model of the geology immediately surrounding the detector as well as the detector shielding. Additionally, due to the fact that the detector is located only a small distance into the Earth's crust the path length through any one of the aforementioned layers varies significantly with the angle of approach of the incoming particle, so the damping factor must be independently calculated for every angle of approach. Figures 4.3 and 4.4

show how the damping factor and velocity distribution vary for different angles of approach, Fig. 4.2 shows the coordinate system that is used to calculate the damping parameter.

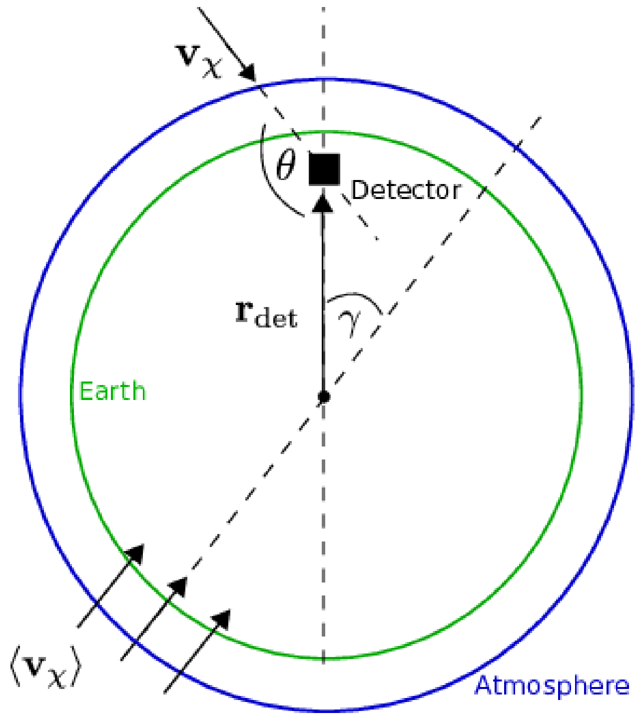

Figure 4.2: The coordinate system used to calculate the damping factor

To have an accurate model of the damping which occurs it is important to have models of the local geology as well as the experiment shielding. Acquiring a useful model of the geology requires consulting with geologists both to get accurate mineral maps of the area as well as to convert the mineral maps in to chemical maps, since what we really care about is the distribution of different nuclear species. Fig. 4.5 shows the geology around the Soudan mine broken up into different radial segments.

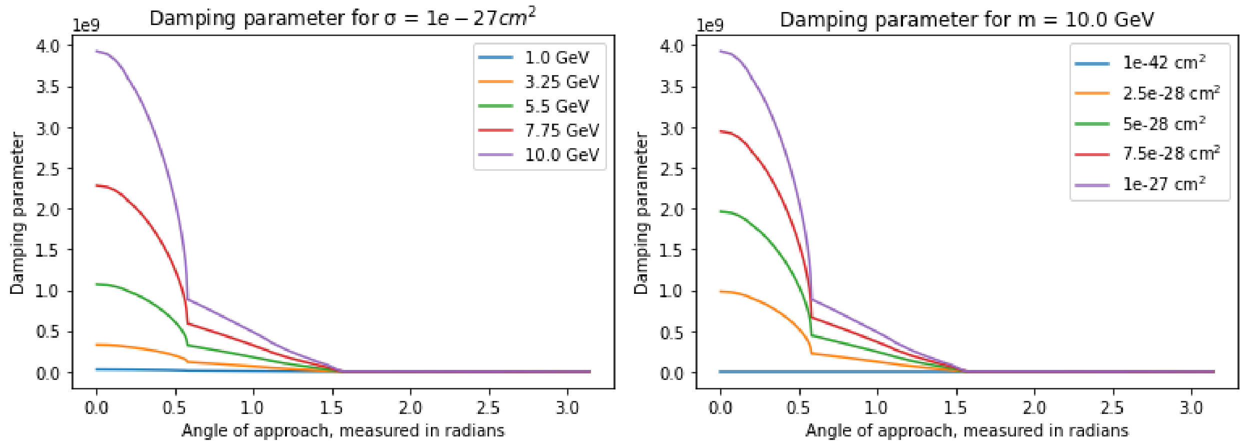

Figure 4.3: The variation of the damping parameter with the angle of approach shown for a fixed cross section and linearly varied mass(left) and a fixed mass and linearly varied cross section(right). We can see that the parameter is linear in cross section and depends exponentially on the mass. We can also see the features of the model of the Earth used for these calculations. The first kink represents the boundary between the core of the Earth and the mantle, and the second kink represents when the dark matter only passes through the rock around the detector, which is why the parameter has a nearly constant non-zero value there.

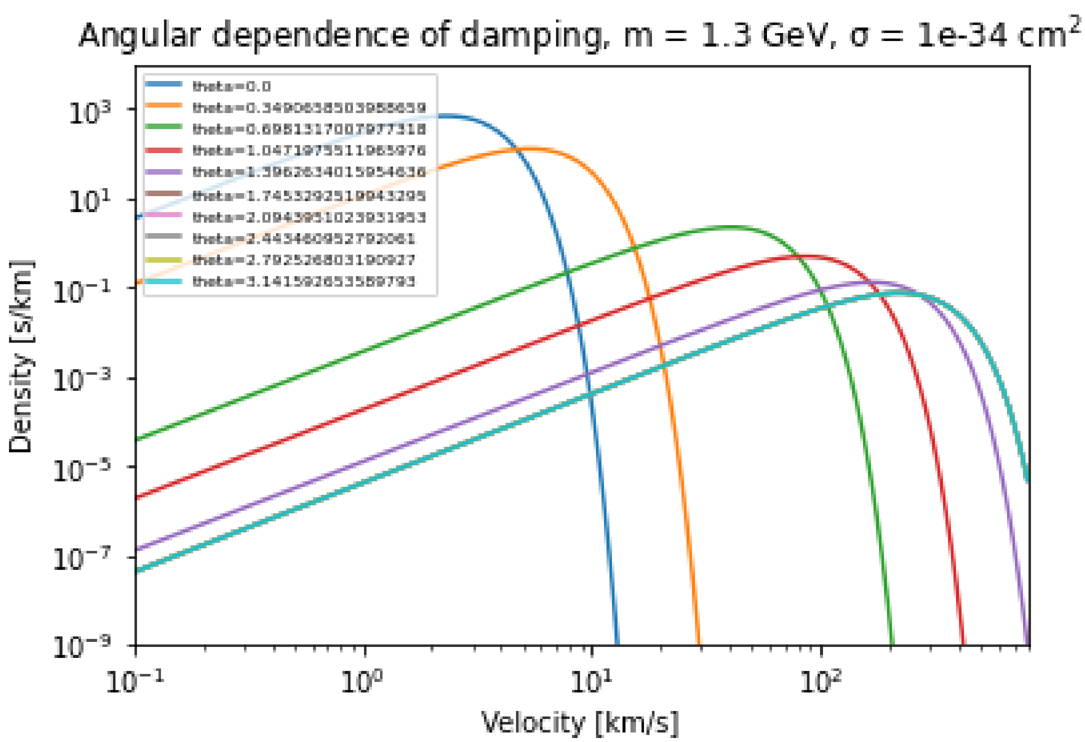

Figure 4.4: How the different velocity distributions vary with their angle of approach to the detector.

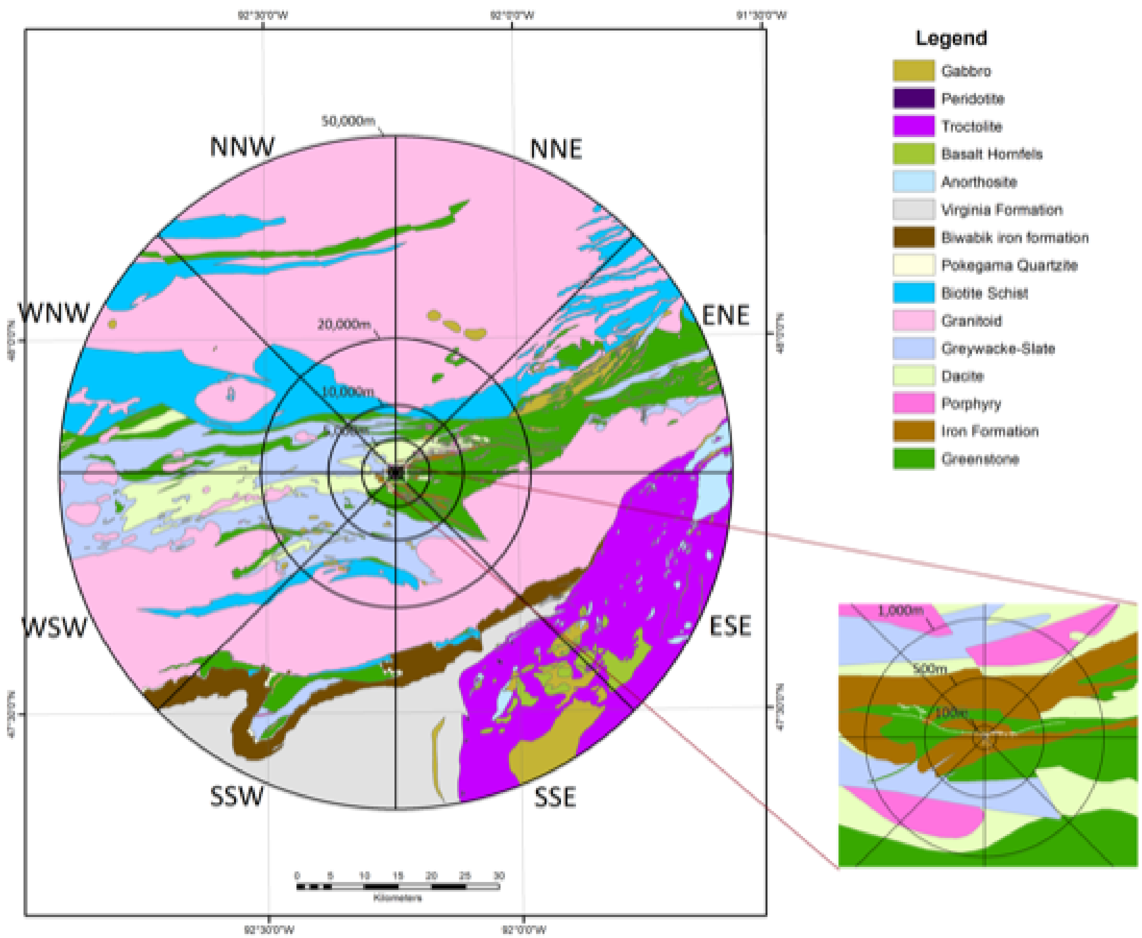

Figure 4.5: Geology surrounding the Soudan mine

CHAPTER 5

Profile Likelihood Analysis

5.1. Likelihood functions

5.1.1. General Introduction

For some random variable x, the probability density function $f(x)$ is defined such that when it is integrated between two values a and b of x it gives the probability of measuring x to have a value between a and b. Now if we parameterize the function f by some parameter θ, varying theta will give us different probability distributions for the random variable x, so we can write $f(\theta|x)$ which tells us the probability of measuring any value for the random variable x if there is a specified value for θ. This description still holds if either or both of θ and x represent sets of variables instead of just one. One physical example of this is the for a set of identical particles in a box, which is parameterized by the mass and temperature of the particles, and ranges over values of velocity, in addition to depending on the Boltzmann constant k_b:

$$f(v|m,T) = (\frac{m}{2\pi k_b T})^{\frac{3}{2}} 4\pi v^2 e^{-\frac{mv^2}{2k_b T}} \tag{5.1}$$

If we take the same equation and instead flip it such that we have already measured one value(s) for the random variable but we do not know what the value(s) of θ are we arrive at the function $\mathcal{L}(\theta|x)$ which tells us the relative likelihood of having measured x to have some specified value for different value(s) of θ.

We can then ask the question of which value(s) for θ are the most likely to have produced our observation.

A very common case is to have a mix of parameters whose values are truly unknown and parameters whose values are known only to some finite precision and so themselves follow a probability distribution. In an experiment the first type of parameter corresponds to the thing you are trying to measure the value of and the second type of parameter corresponds to quantities in the experiment which must be measured to conduct the core measurement but which aren't the quantity of interest. The second type of parameter are commonly referred to as nuisance parameters.

Going back to the example given earlier of the Maxwell-Boltzmann distribution for the speeds of particles in a box, if we have measured the distribution of speeds but do not know what the particle mass is, we would need to measure the temperature of the particles in the box in some other way in order to determine what the most likely mass of the particles is. Because any measurement of the temperature will be imperfect, we account for our level of knowledge of the temperature by writing down its own probability distribution $f(T)$, which describes the relative probabilities of measuring the temperature to have any given value. The pdf for our experiment is then the product of the original speed distribution with the temperature distribution, and so the likelihood becomes $\mathcal{L}(m, T|v) = f(v|m, T) \times f(T)$ where $f(T)$ is called the constraint term corresponding to temperature. It is also not uncommon for multiple nuisance parameters to be correlated with each other, and in that case the distribution which is used to describe them will incorporate a covariance matrix instead of a single number describing the uncertainty on the measurement of each parameter.

5.1.2. The Likelihood function for this analysis

Since the likelihood function has many pieces to it, we will begin this section with a table of all its variables:

Variable	Definition
N	number of events in data
i	iterator over N data events
E_i	energy of event i
ν_{x}	number of signal events
f_X	signal PDF
b	iterator over non-surface backgrounds: Ge-71, Ga- $68, \mathrm{Zn}-65, \mathrm{Fe}-55$, Compton, H-3
ν_b	number of events in background b
f_b	PDF of background b
sb	iterator over surface backgrounds: SH,GZ, TL (TL is R3 only)
ν_{sb}	number of events in surface background sb
ρ_{sb}	event density of surface background sb
k	iterator over systematic nuisance parameters
x_k	value of parameter k
μ_k	expected value of parameter k
σ_k	uncertainty of parameter k
V	variance matrix, aka $(\sigma_k)^2$
d	dimension of Gaussian constraint
s_k	surface background morphing parameter
S	covariance matrix constraining morphing of surface backgrounds
r_k	resolution parameter
R	covariance matrix constraining resolution
Ξ	efficiency morphing parameter (one parameter, no iterator)
θ_Y	Nuclear yield uncertainty in units of standard deviation

Table 5.1: Table of the variables used in the likelihood function

The experiment consists of N data points, and so it is actually N different measurements of the energy of an event. For each measurement, the corresponding pdf is a sum of the dark matter signal pdf $f_\chi(E)$ and the sum of the pdfs for each of the background sources $\sum_b f_b(E)$ where E is the energy of an event. Since there were N total events, the pdfs for each event are multiplied together, so the portion of the likelihood function determined by the signal and background models is:

$$\mathcal{L}_{model} = \mathcal{L}_{\chi,b} = \prod_{i=1}^{N} \left[f_\chi(E_i) + \sum_b f_b(E_i) \right] \tag{5.2}$$

Additionally, this is a counting experiment, where each event is one count, and so the total number of events follows a Poisson distribution which incorporates information about the expected number of events from each model:

$$\mathcal{L}_{\text{poiss}} = \left[\nu_\chi + \sum_b \nu_b \right]^N \times \frac{\exp\left[-\left(\nu_\chi + \sum_b \nu_b \right) \right]}{N!} \tag{5.3}$$

Finally, as discussed in Sec. 5.1.1 each nuisance parameter discussed in earlier chapters of this thesis has a corresponding constraint term. In our case the nuisance parameters are the morphing parameters for each of the surface backgrounds and for the efficiency, the parameters A, B and C from Eq. 3.8 which describe the energy resolution of the detector, and Lindhard k which is used to describe the ionization yield. These constraint terms take the general form:

$$\mathcal{L}_{\text{constr.}} = \frac{1}{\sqrt{2\pi\sigma_k^2}} \times \exp\left(-\frac{(x_k - \mu_k)^2}{2\sigma_k^2} \right) = \frac{1}{(2\pi)^{d/2} |\boldsymbol{V}|^{1/2}} \times \exp\left(-\frac{1}{2} (x_k - \mu_k)^T \boldsymbol{V}^{-1} (x_k - \mu_k) \right) \tag{5.4}$$

Putting this all together, the full likelihood function is a product of all three types of term:

$$\mathcal{L} = \mathcal{L}_{poiss} \times \mathcal{L}_{\chi,b} \times \mathcal{L}_{constr} \tag{5.5}$$

Because the likelihood is a probability of many probabilities which are much smaller than one it tends to take a very small value and so it is more convenient to work with its natural logarithm. Additionally, since we are only concerned with maximizing the likelihood function we can drop any terms which are constant. Taking the logarithm of $\mathcal{L}$ and expanding it out into greater detail, we arrive at the full function which was used for this analysis:

$$
\begin{aligned}
&\left[\ln\left(\mathcal{L}^{R3}_{\text{poiss}}\right) + \ln\left(\mathcal{L}^{R3a}_{\chi,b,sb}\right) + \ln\left(\mathcal{L}^{R3b}_{\chi,b,sb}\right)\right] + \ln\left(\mathcal{L}^{R3}_{\text{surf } f}\right) + \ln\left(\mathcal{L}^{R3a}_{\text{res}}\right) + \ln\left(\mathcal{L}^{R3b}_{\text{res}}\right) + \ln\left(\mathcal{L}^{R3a}_{\text{eff}}\right) + \\
&\ln\left(\mathcal{L}^{R3b}_{\text{eff}}\right) + \ln\left(\mathcal{L}_{Y}\right) = \\
&-\left(\nu^{R3}_{\chi} + \sum_{b} \nu^{R3}_{b} + \sum_{sb} \nu^{R3}_{sb}\right) + \sum_{i=1}^{N^{R3a}} \ln\left[\nu^{R3}_{\chi} f^{R3a}_{\chi}\left(E_i\right) + \sum_{b} \nu^{R3}_{b} f^{R3a}_{b}\left(E_i\right) + \sum_{sb} \rho^{R3a}_{sb}\left(E_i\right)\right] \\
&+ \sum_{i=1}^{N^{R3b}} \ln\left[\nu^{R3}_{\chi} f^{R3b}_{\chi}\left(E_i\right) + \sum_{b} \nu^{R3}_{b} f^{R3b}_{b}\left(E_i\right) + \sum_{sb} \rho^{R3b}_{sb}\left(E_i\right)\right] \\
&- \frac{1}{2}\sum_{k=1}^{3}\left[\left(s^{R3}_{k} - \mu^{R3}_{k}\right)^{T} \boldsymbol{S}^{-1}_{R3}\left(s^{R3}_{k} - \mu^{R3}_{k}\right)\right] \\
&- \frac{1}{2}\sum_{k=1}^{3}\left[\left(r^{R3a}_{k} - \mu^{R3a}_{k}\right)^{T} \boldsymbol{R}^{-1}_{R3a}\left(r^{R3a}_{k} - \mu^{R3a}_{k}\right)\right] - \frac{1}{2}\sum_{k=1}^{3}\left[\left(r^{R3b}_{k} - \mu^{R3b}_{k}\right)^{T} \boldsymbol{R}^{-1}_{R3b}\left(r^{R3b}_{k} - \mu^{R3b}_{k}\right)\right] \\
&- \frac{\left(\Xi^{R3a} - \mu^{R3a}\right)^2}{2\left(\sigma^{R3a}_{\Xi}\right)^2} - \frac{\left(\Xi^{R3b} - \mu^{R3b}\right)^2}{2\left(\sigma^{R3b}_{\Xi}\right)^2} \\
&- \frac{\left(\theta_{Y} - 0\right)^2}{2 * 1^2}
\end{aligned}
\tag{5.6}
$$

5.2. The Limit Calculation

An obvious consequence of the information discussed in section 5.1.1 is that one can compare two hypotheses and see which one is more likely. On its face this still presents a problem, however, because the hypothesis which maximizes the likelihood function is not always the hypothesis which accurately describes the underlying physics, just as when one measures the height of a person they are not always as tall as the average person. What is needed is a way of establishing a threshold for some comparison between the likelihoods corresponding to two hypotheses such that we can reject one. Thankfully this problem is solved by an extremely convenient result by Samuel Wilks [40], which states that for the test statistic q defined as:

$$q = -2\ln\left(\frac{\mathcal{L}(\theta_1|x)}{\mathcal{L}(\theta_2|x)}\right) \tag{5.7}$$

the distribution of q approaches the χ^2 distribution with the number of degrees of freedom equal to the number of parameters in θ if the hypothesis θ_1 is true. This allows us to calculate a value for q that corresponds to a 90% confidence level, and when q rises above that value we reject θ_1.

Typically, one is interested in the question of whether the data is compatible with a hypothesis where one or more of the parameters in θ have some specific fixed value, so hypothesis θ_2 is the set of values of the parameters θ which maximize the value of $\mathcal{L}$, and θ_1 corresponds to the case where $\mathcal{L}$ is maximized while holding one or more of the parameters constant. For most dark matter experiments, the parameter held constant in θ_1 would be the cross section σ of the dark matter particle, and the mass m would be held constant in both θ_1 and θ_2, with the process repeated for many masses within the range of dark matter masses that are capable of causing an event in the detector.

In the case that there is no discovery, q is calculated for different values of the mass and interaction cross section and the places where it drops below the confidence level correspond to the parts of parameter space that have been excluded, an example scan of this nature is shown below.

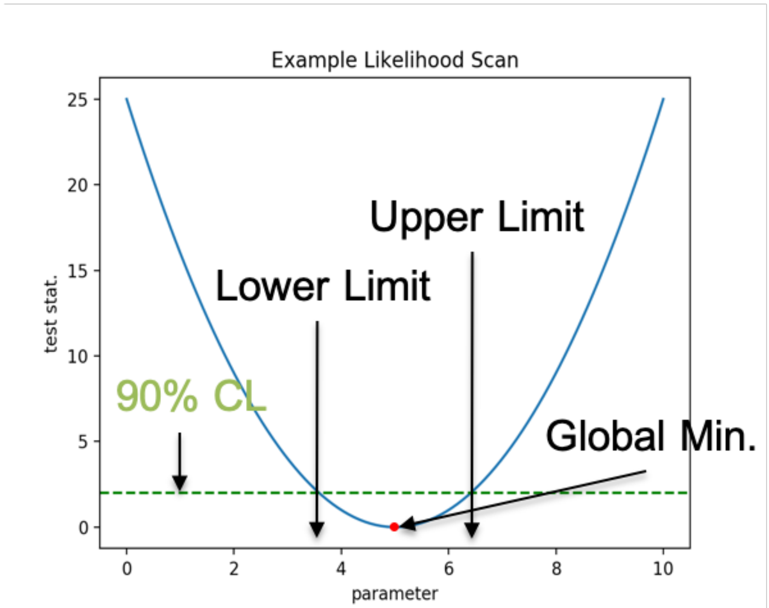

Figure 5.1: an example scan of a test statistic through parameter space. The red point is the unconditional best fit

This choice of parameters to scan over is problematic for this analysis due to the damping effects discussed in chapter 6. For a given mass of dark matter particle, the expected number of events increases linearly with cross section until it reaches a threshold and eventually falls back down to 0. This means that, if m is held constant and a scan is performed over σ where $\mathcal{L}$ is maximized at each new value of σ, there q will have two minima, which is an indication that the parameter over which the test statistic was scanned is inadequate to capture the nature of the data. This can be thought of as due to the fact that the damping introduces a correlation between the shape of the velocity distribution, and thus the expected event rate, and its normalization, so varying σ is really varying two variables at once which, is problematic.

Instead of specifying m and σ and then minimizing q, the scan was performed once for every point in (m,σ) parameter space with number of signal events as the variable which was scanned over. For each point the expected number of events was calculated and compared to the number of events at which q crossed the confidence level and if the expected number of events was smaller than that upper limit, that point in parameter space was deemed compatible with the data and was not part of the excluded region. Two example scans are shown below.

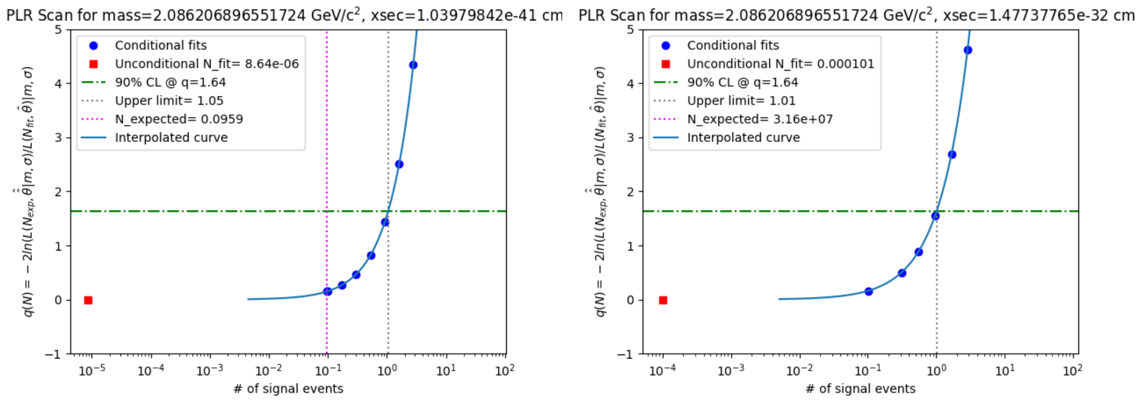

Figure 5.2: Two example scans, one showing a point included (left), one excluded (right)

This new choice of scanning parameter resolves the issue of having more than one local minimum value of q, and allows for the creation of an exclusion band, or an enclosed region of parameter space which corresponds to dark matter particles which would have been found by the experiment if dark matter existed at those points in parameter space.

Chapter 6

Results

The result of the process described in Sec. 5.2 is a band of points in parameter space for which it can be stated with 90% confidence that in CDMSlite R3 data, a dark matter signal was not observed, shown below.

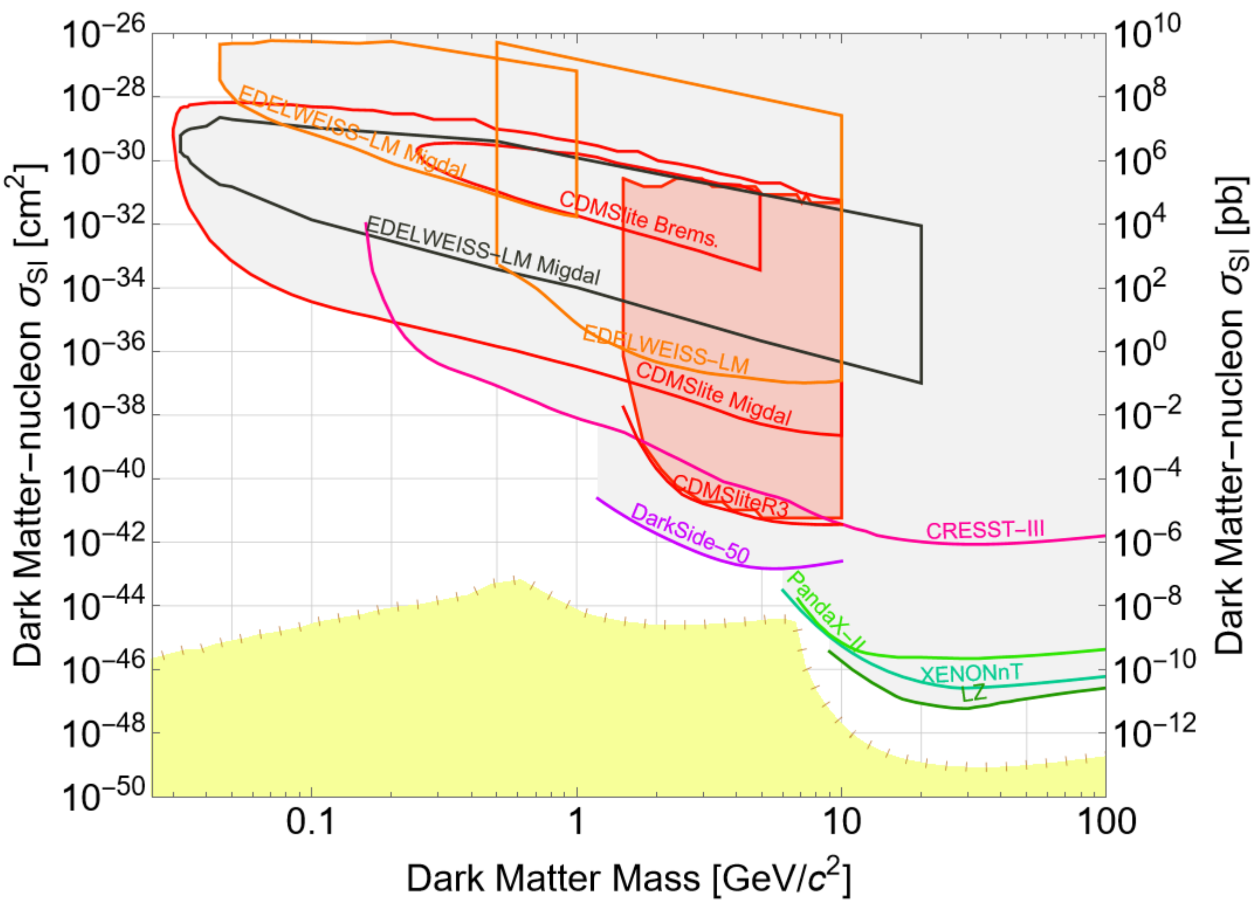

Figure 6.1: The updated exclusion band for CDMSlite run 3 (shaded in red), along side the limits set by a selection of other recent experiments, as well as the neutrino floor shown in yellow

These new limits line up very closely with the lower limits that had been previously calculated for CDMSlite run 3, which was expected since that limit falls into the region of parameter space where the damping effects actually are negligible. Similarly it also lines up very closely with the inelastic upper limits from [41] and the most recent upper limits from EDELWEISS (shown in black). This is also to be expected since the inelastic channels which have been previously examined are also products of nuclear recoils, and the damping effect causes a very sharp drop off in the rate of scattering events for high-cross section dark matter particles. The result of the drop off being so steep is that, as one raises the cross section of a hypothetical dark matter particle, the expected event rates for both types of processes become sow low that the particle is undetectable almost as soon as the damping effect becomes relevant at all. The limits obtained here fall solidly in the already excluded region from Fig. 1.5, so net effect of this is that these limits do not on their own add to or remove from the already explored regions of parameter space. However applying these techniques to experiments which previously did not take overburden effects into account may well open up areas of unexplored parameter space, and applying these techniques to future experiments which are sensitive to lighter mass dark matter will prevent any areas of parameter space from being improperly excluded in the future. In particular, since the lower limits obtained from cosmological constraints are higher for larger dark matter masses, the application of these techniques to liquid noble experiments which are sensitive to heavier dark matter particles may be more likely to yield previously unnoticed windows of unexplored parameter space.

6.1. Outlook

This analysis was a follow-up to the work done using inelastic channels to search for dark matter in CDMSlite R3 data, as well as the original profile likelihood analysis of the R3 [41,42]. While this work did not put new upper lmits on any portion of parameter space, that does not preclude the application of this technique to experiments which are sensitive to dark matter masses below or above the range afforded by this data from doing so. With this in mind, the natural continuation to this work would be to apply the same techniques used here to the upcoming SuperCDMS SNOLAB experiment, as that is expected to have sensitivity at significantly lower masses than SuperCDMS Soudan did in either its iZIP or HV configurations [43]. The main work involved in that would be the acquisition of a chemical map of the geology around the SNOLAB site and in modeling the detector shielding, since although as mentioned above this analysis is not strongly sensitive to the geology of the experiment site, it is nonetheless still somewhat sensitive and a map of the geology is needed to obtain a precise upper limit. Additionally, these results demonstrate that when direct detection experiments begin pushing into the low mass region of unexplored parameter space from Fig. 1.5 that there will be a need for more surface, upper atmosphere, and space-based experiments than we currently see in order to close the areas of parameter space which will be unexplorable by underground experiments.

BIBLIOGRAPHY

[1] W. Thomson and B. Kelvin, *Baltimore Lectures on molecular dynamics and the Wave Theory of Light: Founded on mr. A.S. Hathaway's stenographic report of twenty lectures delivered in Johns Hopkins University, Baltimore, in October 1884: Followed by twelve appendices on Allied subjects*. Cambridge Universiy Press, 1904. 1

[2] F. Zwicky, *Die rotverschiebung von extragalaktischen nebeln*, *Helvetica Physica Acta* **6** 110–127. 1

[3] F. Zwicky, *On the Masses of Nebulae and of Clusters of Nebulae*, **86** (Oct., 1937) 217. 1

[4] V. Rubin and W. Ford, Jr, "Rotation of the andromeda nebula from a spectroscopic survey of emission regions, apj 159." 1

[5] V. C. Rubin, J. Ford, W. K. and N. Thonnard, *Extended rotation curves of high-luminosity spiral galaxies. IV. Systematic dynamical properties, Sa -¿ Sc.*, **225** (Nov., 1978) L107–L111. 1

[6] K. Begeman, A. Broeils and R. Sanders, *Extended rotation curves of spiral galaxies: dark haloes and modified dynamics*, *Monthly Notices of the Royal Astronomical Society* **249** 523. ix, 2

[7] *Planck 2013 results. i. overview of products and scientific results, astron*, *Astrophys* **571** 1,. 3

[8] *Planck 2015 results*, *XIII. Cosmological parameters, 1502.01589* **xv, 11** 12. 3

[9] D. Clowe, M. Bradac, A. Gonzalez, M. Markevitch, S. Randall and C. Jones, *A direct empirical proof of the existence of dark matter, astrophys*, *J* **648** 109– 113, – 0608407. ix, 3, 4

[10] D. S. Graff and K. Freese, *Analysis of a [ITAL]hubble space telescope[/ITAL] search for red dwarfs: Limits on baryonic matter in the galactic halo*, *The Astrophysical Journal* **456** (jan, 1996) . 4

[11] G. Steigman and M. Turner, *Cosmological constraints on the properties of weakly interacting massive particles*, *Nuclear Physics B* **253** 375–386 16. 5

[12] T. Undagoitia and L. Rauch, *Dark matter direct-detection experiments*, *J. Phys* **G43** . ix, 7, 8

[13] E. Armengaud, C. Augier, A. Benoî t, L. Bergé, T. Bergmann, J. Blümer et al., *Search for low-mass WIMPs with EDELWEISS-II heat-and-ionization detectors*, *Physical Review D* **86** (sep, 2012) . 7

[14] A. Abdelhameed, G. Angloher, P. Bauer, A. Bento, E. Bertoldo, C. Bucci et al., *First results from the CRESST-III low-mass dark matter program*, *Physical Review D* **100** (nov, 2019) . 7

[15] J. Liu, X. Chen and X. Ji, *Current status of direct dark matter detection experiments*, *Nature Physics* **13** (mar, 2017) 212–216. 8

[16] J. Bovy and S. Tremaine, *ON THE LOCAL DARK MATTER DENSITY*, *The Astrophysical Journal* **756** (aug, 2012) 89. 10

[17] S. Sharma, J. Bland-Hawthorn, J. Binney, K. C. Freeman, M. Steinmetz, C. Boeche et al., *KINEMATIC MODELING OF THE MILKY WAY USING THE RAVE AND GCS STELLAR SURVEYS*, *The Astrophysical Journal* **793** (sep, 2014) 51. 10

[18] M. C. Smith, G. R. Ruchti, A. Helmi, R. F. G. Wyse, J. P. Fulbright, K. C. Freeman et al., *The RAVE survey: constraining the local galactic escape speed*, *Monthly Notices of the Royal Astronomical Society* **379** (aug, 2007) 755–772. 10

[19] J. Lewin and P. F, *Smith, review of mathematics, numerical factors, and corrections for dark matter experiments based on elastic nuclear recoil, astropart*, *Phys* **6** 87–112. 11

[20] M. A. Buen-Abad, R. Essig, D. McKeen and Y.-M. Zhong, *Cosmological constraints on dark matter interactions with ordinary matter*, *Physics Reports* **961** (may, 2022) 1–35. ix, 12

[21] SuperCDMS Collaboration collaboration, M. F. Albakry, I. Alkhatib, D. Alonso-González, D. W. P. Amaral, T. Aralis, T. Aramaki et al., *Search for low-mass dark matter via bremsstrahlung radiation and the migdal effect in supercdms*, *Phys. Rev. D* **107** (Jun, 2023) 112013. 12

[22] C. collaboration, D. Abrams, D. Akerib, M. Armel-Funkhouser, L. Baudis, D. Bauer et al., *Exclusion limits on the wimp-nucleon cross section from the cryogenic dark matter search*, *Phys. Rev* **D 66** 122003 50. 13

[23] C. collaboration, D. Akerib, M. Attisha, L. Baudis, D. Bauer, A. Bolozdynya et al., *Low-threshold analysis of cdms shallow-site data*, *Phys. Rev* **D 82** 122004 50. 13

[24] D. Akerib, *Installation and commissioning of the cdmsii experiment at soudan*, *Nucl. Instrum. Meth* **A520** 116–119 50. 13

[25] C. collaboration and D. Akerib, *First results from the cryogenic dark matter search in the soudan underground lab*, *Phys. Rev. Lett* **93** – 0405033. 13

[26] M. Pyle, "Optimizing the design and analysis of cryogenic semiconductor dark matter detectors for maximum sensitivity." 13

[27] R. Bunker, "A low-threshold analysis of data from the cryogenic dark matter search experiment." 14

[28] J. Sander, "Results from the cryogenic dark matter search using a chi squared analysis." ix, 15

[29] *Search for low-mass weakly interacting massive particles using voltage-assisted calorimetric ionization detection in the supercdms experiment*, *Phys. Rev. Lett* **112** 041302,. 18

[30] J. Lindhard, V. Nielsen, M. Scharff and P. Thomsen, *Integral equations governing radiation effects*, vol. 33. notes on atomic collisions. 20

[31] D. Barker, W. Wei, D. Mei and C. Zhang, *Ionization efficiency study for low energy nuclear recoils in germanium, astropart*, *Phys* **48** 5. 20

[32] J. Filippini, "Supercdms internal document: Hunting for 66.7 and 511 kev ge peaks." 21

[33] M. Pepin, "Low-mass dark matter search results and radiogenic backgrounds for the cryogenic dark matter search." ix, 22, 24

[34] W. Page, "Searching for low-mass dark matter with supercdms soudan detectors." 25

[35] D. collaboration, A. Aguilar-Arevalo, D. Amidei, X. Bertou, M. Butner, G. Cancelo et al., *Search for low-mass wimps in a 0.6 kg day exposure of the damic experiment at snolab*, *Phys. Rev* **D 94** . 27

[36] J. Allison, K. Amako, J. Apostolakis, P. Arce, M. Asai, T. Aso et al., *Recent developments in geant4*, *Nuclear Instruments and Methods in Physics Research Section A: Accelerators, Spectrometers, Detectors and Associated Equipment* **835** (2016) 186–225. 27

[37] J. Allison, K. Amako, J. Apostolakis, H. Araujo, P. Arce Dubois, M. Asai et al., *Geant4 developments and applications*, *IEEE Transactions on Nuclear Science* **53** (2006) 270–278. 27

[38] S. Agostinelli, J. Allison, K. Amako, J. Apostolakis, H. Araujo, P. Arce et al., *Geant4—a simulation toolkit*, *Nuclear Instruments and Methods in Physics Research Section A: Accelerators, Spectrometers, Detectors and Associated Equipment* **506** (2003) 250–303. 27

[39] T. Emken and C. Kouvaris, *How blind are underground and surface detectors to strongly interacting dark matter?*, *Phys. Rev* **D 97** 123. x, 38, 40

[40] S. Wilks, *The large-sample distribution of the likelihood ratio for testing composite hypotheses*, *Ann. Math. Statist* **9 (03** 60–62 131. 49

[41] M. F. Albakry, I. Alkhatib, D. Alonso, D. W. P. Amaral, T. Aralis, T. Aramaki et al., *A search for low-mass dark matter via bremsstrahlung radiation and the migdal effect in supercdms*, 2023. 53

[42] *Search for low-mass dark matter with cdmslite using a profile likelihood fit*, *Phys. Rev* **D99** 104. 53

[43] R. Agnese, A. Anderson, T. Aramaki, I. Arnquist, W. Baker, D. Barker et al., *Projected sensitivity of the SuperCDMS SNOLAB experiment*, *Physical Review D* **95** (apr, 2017) . 54